

AWARD NUMBER: W81XWH-16-1-0565

TITLE: Engineer Synthetic Tumor Recruited Immunocellular Therapy (STRICT)

PRINCIPAL INVESTIGATOR: Timothy Lu

CONTRACTING ORGANIZATION: Massachusetts Institute of Technology  
Cambridge, MA 02139

REPORT DATE: September 2017

TYPE OF REPORT: Annual

PREPARED FOR: U.S. Army Medical Research and Materiel Command  
Fort Detrick, Maryland 21702-5012

DISTRIBUTION STATEMENT: Approved for Public Release;  
Distribution Unlimited

The views, opinions and/or findings contained in this report are those of the author(s) and should not be construed as an official Department of the Army position, policy or decision unless so designated by other documentation.

REPORT DOCUMENTATION PAGE				Form Approved OMB No. 0704-0188	
Public reporting burden for this collection of information is estimated to average 1 hour per response, including the time for reviewing instructions, searching existing data sources, gathering and maintaining the data needed, and completing and reviewing this collection of information. Send comments regarding this burden estimate or any other aspect of this collection of information, including suggestions for reducing this burden to Department of Defense, Washington Headquarters Services, Directorate for Information Operations and Reports (0704-0188), 1215 Jefferson Davis Highway, Suite 1204, Arlington, VA 22202-4302. Respondents should be aware that notwithstanding any other provision of law, no person shall be subject to any penalty for failing to comply with a collection of information if it does not display a currently valid OMB control number. <b>PLEASE DO NOT RETURN YOUR FORM TO THE ABOVE ADDRESS.</b>					
1. REPORT DATE September 2017		2. REPORT TYPE Annual		3. DATES COVERED 1 Sep 2016- 31 Aug 2017	
4. TITLE AND SUBTITLE  Engineer Synthetic Tumor Recruited Immunocellular Therapy (STRICT)				5a. CONTRACT NUMBER	
				5b. GRANT NUMBER W81XWH-16-1-0565	
				5c. PROGRAM ELEMENT NUMBER	
6. AUTHOR(S) Timothy Lu  timlu@mit.edu				5d. PROJECT NUMBER	
				5e. TASK NUMBER	
				5f. WORK UNIT NUMBER	
7. PERFORMING ORGANIZATION NAME(S) AND ADDRESS(ES) Massachusetts Institute of Technology 77 Massachusetts Ave, Cambridge, MA 02139-4301				8. PERFORMING ORGANIZATION REPORT NUMBER	
9. SPONSORING / MONITORING AGENCY NAME(S) AND ADDRESS(ES)  U.S. Army Medical Research and Materiel Command Fort Detrick, Maryland 21702-5012				10. SPONSOR/MONITOR'S ACRONYM(S)	
				11. SPONSOR/MONITOR'S REPORT NUMBER(S)	
12. DISTRIBUTION / AVAILABILITY STATEMENT  Approved for Public Release; Distribution Unlimited					
13. SUPPLEMENTARY NOTES					
14. ABSTRACT The purpose of this project is to build a versatile Tumor Recruited Immunocellular Therapy (STRICT) system for prostate cancer. In the research period, we have validated that STRICT system have the potential to trigger robust immunotherapy. The majority of this validation is performed in an ovarian cancer model in vitro and in vivo. With ovarian cancer model, we have identified the key circuit component for building highly tumor-specific immunomodulatory system. We also identified the optimal circuit architecture for this system. In addition, we have created a library of sensors that can be used to detect multiple different cancer types. Currently, we are able to find new sensors for building this system toward treating prostate cancer. The next step forward is to validate whether combining the sensors with the optimal circuit architecture, the system remains highly specific to prostate cancer cells but not to other major tissue types in vitro. After the circuit specificity has been validated, we will identify the minimal percentage of tumor cells that need to be targeted by STRICT system to mediate in vivo efficacy. Furthermore, we will determine whether STRICT system can eliminate metastatic tumors via systemic delivery.					
15. SUBJECT TERMS synthetic gene circuit; cancer immunotherapy, prostate cancer					
16. SECURITY CLASSIFICATION OF:			17. LIMITATION OF ABSTRACT	18. NUMBER OF PAGES	19a. NAME OF RESPONSIBLE PERSON
a. REPORT	b. ABSTRACT	c. THIS PAGE			USAMRMC
U	U	U	UU	72	19b. TELEPHONE NUMBER (include area code)

## Table of Contents

	<u>Page</u>
1. Introduction.....	4
2. Keywords.....	4
3. Accomplishments.....	4
4. Impact.....	6
5. Changes/Problems.....	7
6. Products.....	7
7. Participants & Other Collaborating Organizations.....	8
8. Special Reporting Requirements.....	9
9. Appendices.....	9

## 1. INTRODUCTION:

Prostate cancer remains the most common non-cutaneous malignancy in men in USA. Active surveillance can be applied to most patients. However, around 15% of prostate cancer patients are diagnosed with high risk disease, and these patients have significantly higher chances of developing systemic metastasis or local recurrence, therefore more intensive treatment is required. Treatment options, including surgery, radiation therapy, and androgen-deprivation therapy, or their combinations, are often ineffective in a subset of high risk patients. Most patients with high-risk disease relapse after therapy, and there are no effective preventive measures. Immunotherapy holds great potential in treating prostate cancer. However, major challenges remain. We propose an innovative immunotherapy approach to kill tumor cells, one that combines the specificity of gene circuits with the ability of Surface T-cell Engagers (STEs). STEs can trigger antigen-independent T-cell killing of tumor cells *in vitro* and *in vivo*. This approach, Tumor Recruited Immunocellular Therapy (STRICT) is a unique and innovative combination of cancer-detecting gene circuits with anti-cancer immunotherapies. Synthetic gene circuits, administered systemically, will be selectively activated only in cancer cells, resulting in the surface display of STE and the secretion of potent immunomodulatory molecules. The STEs will recruit T cells to target and kill the tumor. Combining the advantages of localized immunotherapy with those of systemic delivery, STRICT would obviate the need for systemic chemotherapy and protect against tumor relapse. In addition, STRICT is expected to overcome the key obstacles associated with other therapies currently available for prostate cancer.

2. **KEYWORDS:** synthetic gene circuit; cancer immunotherapy, prostate cancer

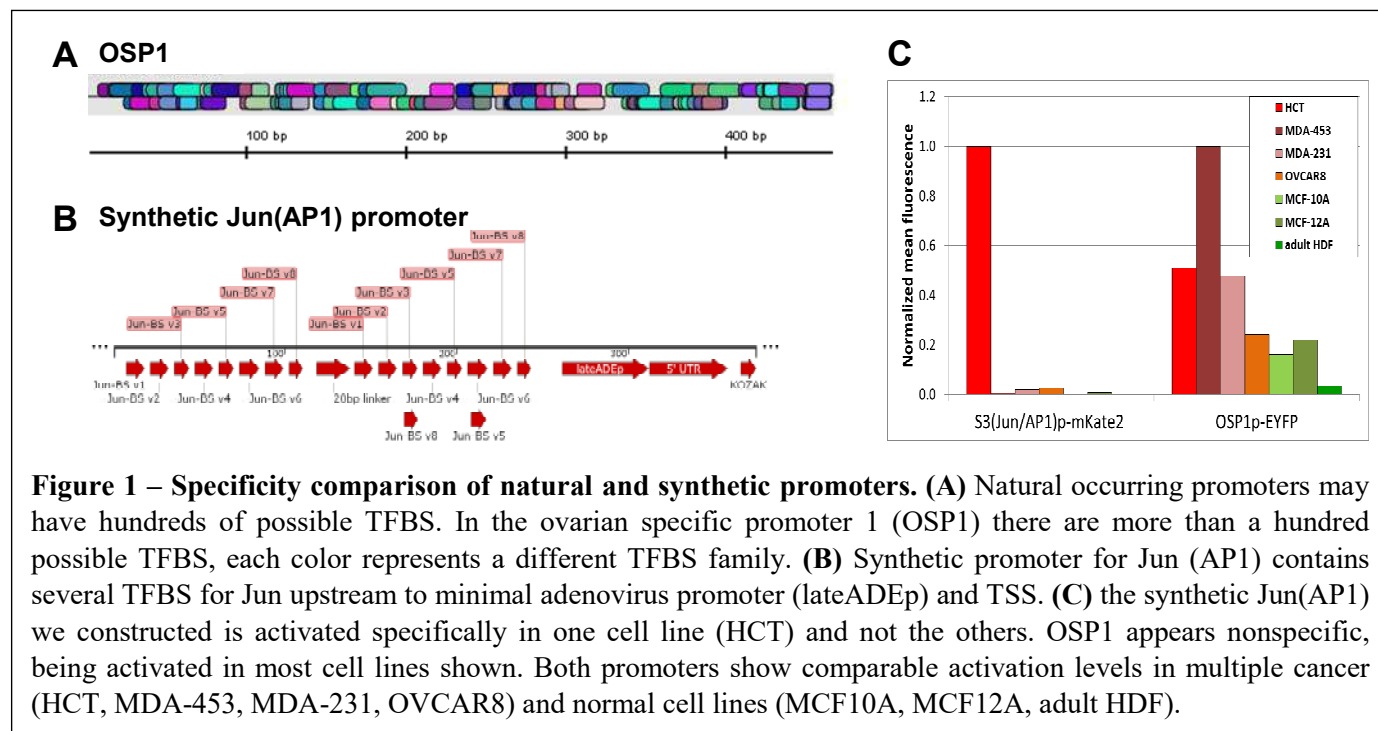
## 3. ACCOMPLISHMENTS:

**What were the major goals of the project?**

	Months	Percentage of Completion
Major Task 1: Create, optimize, and validate cancer-detecting circuits that display Surface T-cell Engagers (STEs) from within tumors.	1-9	75%
Major Task 2: Identify the minimal percentage of tumor cells that need to be targeted by TIGRIS for <i>in vivo</i> efficacy.	9-15	0%
Major Task 3: Determine whether TIGRIS can eliminate metastatic tumors via systemic delivery.	3-36	0%
Major Task 4: Build synthetic safety mechanisms for TIGRIS circuits.	15-30	0%
Major Task 5: Test if TIGRIS can elicit immune memory to protect against future tumor relapse.	15-36	0%

**What was accomplished under these goals?**

The major activities throughout this report period focused on building a versatile Tumor Immunotherapy by Gene-circuit Recruited Immunomodulatory Systems (TIGRIS) for prostate cancer. In this research period, by using ovarian cancer model, we have validated that TIGRIS have the potential to trigger robust immunotherapy in vitro and in vivo (see appendix for an accepted manuscript). We have optimized the key circuit building blocks for creating highly effective RNA-based synthetic gene circuit for tumor-specific immunomodulation. We also optimized circuit architecture that enables this system to be high modular for easy adaptation for treating other cancer type and for future clinical translation. In addition, we have created a method to build synthetic promoters that perform better than native promoters for targeting cancers (Figure 1). These promoters directly serve as sensors for TIGRIS system and we further extend this method to build a library of synthetic promoters ( > 6000 different synthetic promoters) that serve as a sensor library for TIGRIS system. This library can be used to detect multiple different cancer types. Currently, we are able to find new sensors for building this system toward treating prostate cancer (Table 1). The next step forward is to validate whether combining the sensors with the optimal circuit architecture, the system remains highly specific to prostate cancer cells but not to other major tissue types in vitro.



## What opportunities for training and professional development has the project provided?

This project provides extensive training for postdoc fellow Dr. Ming-Ru Wu on designing cancer-detection circuits, optimizing circuit inputs and outputs, and cancer immunotherapy. It also provided Dr. Ming-Ru Wu with hands on experience on working with prostate cancer models.

## How were the results disseminated to communities of interest?

Nothing to report.

#### What do you plan to do during the next reporting period to accomplish the goals?

We will further utilize the identified sensors to build TIGRIS system for prostate cancer. We will validate the system is specific to prostate cancer cells but not normal tissues. In addition, we will identify the minimal percentage of tumor cells that need to be targeted by TIGRIS system to mediate in vivo efficacy. Furthermore, we will determine whether TIGRIS can eliminate metastatic tumors via systemic circuit delivery.

promoter	Transcription factor binding site	MFI (PC3)	Fold to background MFI	MFI (DU145)	Fold to background MFI
1	SPDEF_mus	775	16	513	11
2	MYC	46	1	22	0
3	MYC	49	1	44	1
4	MYC/USF1	47	1	44	1
5	MYCN_mus/CLK_d.melanogaster	47	1	41	1
6	TJ_d.melanogaster (MAFB)	287	6	131	3
7	SPDEF_mus	511	10	588	12
8	FOXA	47	1	41	1
9	MAFK	148	3	80	2
10	FOXA3	416	9	86	2
11	E2F1/E2F4	46	1	43	1
12	E2F	52	1	83	2
13	MAFG	60	1	59	1
14	MAFK	167	3	86	2

**Table 1: Identification of promoters that are active in prostate cancers.** The activity of 14 breast cancer specific promoters were tested on 2 prostate cancer cell lines (PC3, DU145) by lentiviral transduction. MFI = mean fluorescence intensity. Fold to background MFI was calculated by dividing the MFI of individual promoters to the MFI of infection control cells. 2-3 promoters exhibit > 9 fold higher activity than background fluorescence and can be further used to build the TIGRIS system.

#### 4. IMPACT:

##### What was the impact on the development of the principal discipline(s) of the project?

Our data utilizing TIGRIS system for treating ovarian cancer had demonstrated the feasibility and the potential robust efficacy of TIGRIS system. If the adaptation of TIGRIS system to prostate cancer is successful, this technology would represent a major step forward in our ability to eliminate prostate cancer, especially metastatic and recurrent disease, in a scalable and programmable fashion.

##### What was the impact on other disciplines?

Our data highlighted the potential power of utilizing gene circuit to treat unmet clinical needs.

**What was the impact on technology transfer?**

Nothing to report.

**What was the impact on society beyond science and technology?**

Nothing to report.

**5. CHANGES/PROBLEMS**

**Changes in approach and reasons for change**

Nothing to report.

**Actual or anticipated problems or delays and actions or plans to resolve them**

Nothing to report.

**Changes that had a significant impact on expenditures**

Nothing to report.

**Significant changes in use or care of human subjects, vertebrate animals, biohazards, and/or select agents**

Nothing to report.

**Significant changes in use or care of human subjects**

Nothing to report.

**Significant changes in use or care of vertebrate animals**

Nothing to report.

**Significant changes in use of biohazards and/or select agents**

Nothing to report.

**6. PRODUCTS:**

**Publications, conference papers, and presentations**

**Journal publications.**

Nissim L, **Wu MR (Co-first author)**, Pery E, Binder-Nissim A, Suzuki HI, Stupp D, Wehrspaun C, Tabach Y, Sharp PA, and Lu TK. 2017. Synthetic RNA-based immunomodulatory gene circuits for cancer immunotherapy. *Cell* (accepted, awaiting publication); acknowledgement of federal support (yes).

**Books or other non-periodical, one-time publications.**

Nothing to report.

**Other publications, conference papers, and presentations.**

Nothing to report.

**Website(s) or other Internet site(s)**

Nothing to report.

**Technologies or techniques**

Nothing to report.

**Inventions, patent applications, and/or licenses**

Patent submitted by Massachusetts Institute of Technology: Lu et al. (2016) U.S. TUMOR IMMUNOTHERAPY. 62/181906,M0656.70356

**Other Products**

Nothing to report.

**7. PARTICIPANTS & OTHER COLLABORATING ORGANIZATIONS****What individuals have worked on the project?**

Name:	Ming-Ru Wu
Project Role:	Postdoc Researcher
Researcher Identifier (e.g. ORCID ID):	orcid.org/0000-0002-2533-8484
Nearest person month worked:	12
Contribution to Project:	Dr. Wu has been performing designing and optimizing TIGRIS system for prostate cancer
Funding Support:	Department of Defense (W81XWH-16-1-0452).

**Has there been a change in the active other support of the PD/PI(s) or senior/key personnel since the last reporting period?**

Nothing to report.

**What other organizations were involved as partners?**

Nothing to report.

**8. SPECIAL REPORTING REQUIREMENTS**

Nothing to report.



## 9. APPENDICES:

### **Journal publications.**

Nissim L, **Wu MR (Co-first author)**, Pery E, Binder-Nissim A, Suzuki HI, Stupp D, Wehrspaun C, Tabach Y, Sharp PA, and Lu TK. 2017. Synthetic RNA-based immunomodulatory gene circuits for cancer immunotherapy. *Cell* (accepted, awaiting publication); acknowledgement of federal support (yes).

**Date:** Sep 27, 2017  
**To:** "Timothy K Lu" timlu@mit.edu;tim@lugroup.org  
**cc:** cellms@cell.com  
**From:** "Cell Editorial Office" cellms@cell.com  
**Subject:** Cell Editorial Decision CELL-D-17-01314R3

Prof. Timothy Lu  
77 Massachusetts Ave  
NE47-221  
Cambridge MA  
UNITED STATES

Synthetic RNA-based immunomodulatory gene circuits for cancer immunotherapy  
CELL-D-17-01314R3

Sep 27, 2017

Dear Tim,

It is a pleasure to let you know that we will be publishing your paper and that it is being tentatively scheduled for the November 30 issue of Cell. Congratulations on a very interesting story; we are pleased to be bringing it to the attention of our readers. In the next week or so, our Production department will contact you with your online publication date that will be ahead of the print issue date.

At this time, I also wanted to introduce our Managing Editor, Trina Arpin, who heads up the production team that will guide your paper through copyediting, proofing, and publication. They will be contacting you shortly with some initial information on the production process. If you anticipate being unreachable by email at any time between now and the publication date, please send them (tarpin@cell.com) the email address of an alternate author who can rapidly respond to queries from our production department.

In the coming weeks, your assigned copyeditor will be in contact with you concerning queries on the manuscript and PDF proofs. We would greatly appreciate it if you can keep an eye out for emails concerning these finishing steps so that we can move your paper efficiently through to publication. Please note that at this stage we can only allow minor corrective changes to the manuscript, and none that will add or change results or significantly alter the length/style of the title, abstract or manuscript text. If any concerns about this arise, please contact me directly. Please see below for further details about proofs.

A note about press, our general policy with regard to press coverage is that authors are free to talk with the popular press starting one week before publication. Your press office may issue its own press release provided that it is embargoed until 12:00pm NOON EST on the day of online publication (as mentioned above, we'll let you know about the online publication date soon). We also allow authors to discuss their work in press with other scientific journals. Because journals could in principle use that information to speed publication of their own competitive manuscripts, it is best if you refer any inquiries to us. Once the requesting journal has confirmed that they do not have any related work under consideration or in press, we'll be glad to send page proofs with a note of the embargo date.

If your press office wishes to issue a press release, they should contact us in advance for final embargo information. **Please contact our press office at [press@cell.com](mailto:press@cell.com).** Prior to publication, please discuss any possibility of the paper being referenced elsewhere in the literature with the handling editor.

Again, congratulations on a very nice paper. We hope you found the review process to be constructive and are pleased with how the manuscript was handled editorially. We look forward to future exciting submissions from your lab.

Best wishes,  
Sri

Sri Devi Narasimhan, Ph.D.  
Scientific Editor, Cell

**Proofs**

- You should receive PDF proofs 2-3 weeks prior to your publication date. Only printer's errors should be corrected on the page proofs.
- You can expect to receive a link to an online copyright assignment form from our Production Department to authorize publication of your paper.
- **For further clarifications regarding the production process, please contact Trina Arpin ([tarpin@cell.com](mailto:tarpin@cell.com)).**

## Databases

- Authors are encouraged to deposit materials used in their studies to the appropriate repositories for distribution to researchers.
- In addition to the information that is required to be deposited in public databases (as stated in our [Instructions to Authors](#)), we also encourage our authors to contribute additional information to the appropriate databases. For example, papers that include data on biomolecular interactions (e.g., protein-protein, protein-RNA) can be submitted to the [Biomolecular Interaction Network Database](#). For a link to additional databases and repositories, please see the [Distribution of Materials and Data](#) section of our Instructions for Authors.

## Cover Submissions

- Please keep in mind that although the submission may be based on or resemble the figures in the article, it should be both artistic and informative. Feel free to submit several different images for consideration, as we like to have as many images as possible to choose from. In addition, even if not chosen for the cover, your submission may be used on the homepage slider to attract more attention to your paper. The editors make the cover selection based on (1) the aesthetic quality of the image and (2) the scientific scope of the study. Please try to make any submissions interesting and creative.
- For all guidelines, please see our [webpage](#). Here you will also find a cover template that contains the Cell logo and crop lines. You do not have to use the template but are welcome to.

# Synthetic RNA-based immunomodulatory gene circuits for cancer immunotherapy

Lior Nissim<sup>1\*</sup>, Ming-Ru Wu<sup>1\*</sup>, Erez Pery<sup>1</sup>, Adina Binder-Nissim<sup>1</sup>, Hiroshi I. Suzuki<sup>2</sup>, Doron Stupp<sup>3</sup>, Claudia Wehrspaun<sup>1</sup>, Yuval Tabach<sup>3</sup>, Phillip A. Sharp<sup>2,4</sup>, Timothy K. Lu<sup>1,5,6,7,8\*\*</sup>

\*These authors contributed equally to this work

\*\*Corresponding author. Email: [timlu@mit.edu](mailto:timlu@mit.edu)

<sup>1</sup>*Synthetic Biology Group, Research Laboratory of Electronics, Massachusetts Institute of Technology, Cambridge, MA 02139, USA.*

<sup>2</sup>*David H. Koch Institute for Integrative Cancer Research, Massachusetts Institute of Technology, Cambridge, MA 02139, USA.*

<sup>3</sup>*Department of Developmental Biology and Cancer Research, The Institute for Medical Research Israel– Canada, The Hebrew University– Hadassah Medical School, Jerusalem 91120, Israel*

<sup>4</sup>*Department of Biology, Massachusetts Institute of Technology, Cambridge, MA 02139, USA*

<sup>5</sup>*Synthetic Biology Center, Department of Biological Engineering, Massachusetts Institute of Technology, Cambridge, MA 02139, USA.*

<sup>6</sup>*Department of Electrical Engineering and Computer Science, Massachusetts Institute of Technology, Cambridge, MA 02139, USA.*

<sup>7</sup>*Biophysics Program, Harvard University, Boston, MA 02115, USA.*

<sup>8</sup>*Center for Microbiome Informatics and Therapeutics, Massachusetts Institute of Technology, Cambridge, MA 02139, USA.*

## Summary

Despite its success in several clinical trials, cancer immunotherapy remains limited by the rarity of targetable tumor-specific antigens, tumor-mediated immune suppression, and toxicity triggered by systemic delivery of potent immunomodulators. Here we present a proof-of-concept immunomodulatory gene circuit platform that enables tumor-specific expression of immunostimulators, which could potentially overcome these limitations. Our design comprised *de novo* synthetic cancer-specific promoters and, to enhance specificity, an RNA-based AND gate that generates combinatorial immunomodulatory outputs only when both promoters are mutually active. These outputs included an immunogenic cell-surface protein, a cytokine, a chemokine, and a checkpoint inhibitor antibody. The circuits triggered selective T-cell-mediated killing of cancer cells but not of normal cells *in vitro*. In *in vivo* efficacy assays, lentiviral circuit delivery mediated significant tumor reduction and prolonged mouse survival. Our design could be adapted to drive additional immunomodulators, sense other cancers, and potentially to treat other diseases that require precise immunological programming.

## Introduction

The potential of cancer immunotherapy has been demonstrated in several clinical trials. Yet this approach is still limited by several major challenges (Maude et al., 2014; Postow et al., 2015). For example, CAR-T cells and bispecific antibodies should ideally target cell-surface antigens that are exclusively present on tumor cells, since targeting normal tissues can result in severe side effects (Morgan et al., 2010; Sadelain et al., 2013; Satta et al., 2013). However, finding highly tumor-specific surface antigens is difficult, which limits the range of targetable tumors (Hassan and Ho, 2008; Kershaw et al., 2014; Klebanoff et al., 2016; Maude et al., 2014; Morgan et al., 2010). In addition, even when ideal targetable tumor-antigens are available, tumor-mediated immunosuppression can prevent successful immunotherapy by disrupting important immunological functions that are necessary for effective anti-tumor immune responses (Chmielewski et al., 2014; Newick et al., 2016; Rabinovich et al., 2007; Turley et al., 2015). Thus, the lack of targetable tumor-specific antigens and tumor-mediated immunosuppression constitute major challenges for cancer immunotherapy.

Immunostimulatory factors can be utilized to overcome these challenges, but off-target activity often results in severe toxicity (van der Burg et al., 2016). For example, Surface T-cell Engagers (STEs) are artificial immunogenic cell-surface proteins that bind the non-variable regions of the T-cell receptor complex. Consequently, STE expressing cells are designated to T-cell mediated killing, regardless of T-cell receptor antigen specificity (see Figure 1B for our STE design based on membrane-anchored anti-CD3 scFv). Tumor-specific STE expression can substitute for targetable tumor antigens, but must be constrained to cancer cells to avoid damage to healthy tissues (Liao et al., 2003; Liao et al., 2000; Yang et al., 2007). Other immunomodulators, such as chemokines, cytokines and immune checkpoint inhibitors can assist in overcoming tumor-mediated immunosuppression, but have caused severe side effects in clinical trials (Lasek et al., 2014; Leonard et al., 1997; Lin et al., 2014; Postow et al., 2015). Furthermore, individual immunomodulators are frequently insufficient on their own to yield strong anti-tumor efficacy (Mahoney et al., 2015; Morrissey et al., 2016). Combinatorial immunotherapy can provide significantly stronger efficacy, but also increase the risk and severity of adverse effects (Boutros et al., 2016; Carson et al., 2000; Lee et al., 2009; Liao et al., 2003; Liu et al., 2011; Paul et al., 2002). Tumor-localized release of immunomodulators could potentially decrease these systemic

side effects and improve the therapeutic efficacy (Neri and Sondel, 2016; Shukla and Steinmetz, 2016; Tugues et al., 2015), but is challenging. Thus, although various strategies are being explored to overcome this problem, further development is required (Bell and McFadden, 2014; Neri and Sondel, 2016; Shukla and Steinmetz, 2016; Tugues et al., 2015; Zaharoff et al., 2010).

Synthetic biology enables the creation of powerful genetic biological tools for studying, diagnosing, and treating disease (Bacchus et al., 2013; Bojar and Fussenegger, 2016; Fenno et al., 2014; Kotula et al., 2014; Pardee et al., 2016; Schukur and Fussenegger, 2016; Schukur et al., 2015; Wei et al., 2012; Xie et al., 2016). For example, synthetic tumor-targeting gene circuits have been previously designed to target tumor cells with enhanced specificity, but have not leveraged the anti-tumor potential of the immune system, which potentially limits their efficacy (Liu et al., 2014; Morel et al., 2016; Nissim and Bar-Ziv, 2010; Xie et al., 2011). We hypothesized that gene circuits could be designed to achieve tumor-specific production of multiple immunomodulators and thus overcome major obstacles in current immunotherapies (Figure 1A).

Here, we demonstrate the potential of gene circuits for cancer immunotherapy. Tumor-targeting gene circuits often require promoters with high cell-state specificity to function as cancer sensors, which can be hard to find (Selvakumaran et al., 2001; Yun et al., 2008). Moreover, native mammalian promoters can span several kb and are therefore difficult to fit into the limited encoding capacity of many viral vectors. Thus, we constructed compact synthetic promoters *de novo* that exhibited enhanced specificity for human cancer cells compared with previously described endogenous cancer-specific promoters.

Discriminating cancer cells based on the integration of multiple cancer markers significantly enhances targeting specificity (Liu et al., 2014; Morel et al., 2016; Nissim and Bar-Ziv, 2010; Roybal et al., 2016; Xie et al., 2011). Thus, to enhance the circuit selectivity over a single synthetic promoter, we designed a synthetic RNA-based circuit that integrates the activity of two synthetic ovarian-cancer specific promoters and generates output proteins only when both promoters are decidedly active, analogous to a Boolean AND gate. Specifically, input promoter 1 regulates an auto-inhibitory mRNA that encodes the output protein, while input promoter 2 regulates an RNA molecule that relieves the auto-inhibition and thus enables output production. This RNA-based design has the potential to reduce the off-target immunogenic signature of the circuit by minimizing the expression of foreign proteins in normal cells. Immunomodulatory outputs

used in this study include a cell-surface antigen (STE) together with secreted a chemokine that promotes T-cell trafficking to tumor sites (CCL21), a cytokine that supports T-cell activation and expansion (IL12), and an immune checkpoint inhibitor (anti-PD1 antibody), hereafter referred to as the SCIP combination (Lasek et al., 2014; Liao et al., 2003; Liao et al., 2000; Lin et al., 2014; Postow et al., 2015; Yang et al., 2007).

We characterized our circuits with *in vitro* specificity assays using normal and cancer cell lines and *in vivo* efficacy assays using a disseminated ovarian cancer model, which recapitulates advanced human ovarian cancer (Lengyel et al., 2014; Sale and Orsulic, 2006). In addition, we demonstrated that our circuit can be readily modified to target breast cancer cells by replacing the synthetic input promoters. Our circuit design is modular and enables facile construction, testing, and optimization of arbitrary promoter inputs, circuit components, and outputs. The outputs can be any genetically encodable element, including intracellular, secreted, and cell-surface proteins. This flexibility will enable circuits to be optimized using advanced tumor models and patient-derived tumors, which will be important for translation into clinical use. Thus, our programmable immunomodulatory gene circuits have broad potential utility for cancer immunotherapy and studying tumor immunology.

## Results

### *RNA-based AND Gate Circuit*

We first designed and optimized the RNA-based AND gate. We engineered two genetic modules such that each was regulated by a separate promoter (Figure 2A-B). *Module 1* consists of input promoter 1 (“P1”), which regulates the expression of an RNA that encodes two exons of an output protein mKate2 (mK-Ex1, mK-Ex2), separated by a synthetic intronic miRNA (miR1), and perfect match miR1 binding sites (BS(Pe)) downstream to the second exon. Following splicing, the exons are assembled into a mature output mRNA that contains BS(Pe) in the 3’ untranslated region (3’ UTR) while the intron is processed by the cell to produce miR1. Consequently, when only promoter 1 is active, miR1 binds the BS(Pe) sites in the output mRNA and targets it for degradation. Therefore, *Module 1* constitutes an auto-inhibitory loop for the output protein production (Figure 2A). *Module 2* consists of input promoter 2 (“P2”), which regulates a miRNA sponge that consists of multiple bulged complementary miR1 binding sites (BS(B)) and thus acts



as a miR1 shunt that relieves the auto-inhibitory nature of *Module 1* when it is expressed (Figure 2A-B). In this system, the output protein is expressed at a high level only when the promoters regulating both modules are mutually active. However, when only one of the promoters is active or when none of the promoters are active, output protein expression is low.

We systematically optimized various aspects of the miRNA-based mechanism (Figure 3 & Figure S1-3; for further details, see Supplementary Information) (Auyeung et al., 2013; Ebert and Sharp, 2010; Fellmann et al., 2013; Gure et al., 1997; Haraguchi et al., 2009; Kertesz et al., 2007; Rogakou et al., 1998; Suzuki et al., 2015). In *Module 2*, we characterized how the miRNA binding site sequence, expression level, and sponge architecture determines the efficiency of the miR1 sponge (Figure 3 & Figure S1-2). We defined four different states for this circuit: state [0,0] – both *Module 1* and *Module 2* are inactive, [0,1] – *Module 1* is inactive while *Module 2* is active, [1,0] – *Module 1* is active while *Module 2* is inactive, and [1,1] – both *Module 1* and *Module 2* are active (Figure 2B). The ON-OFF ratio for the AND gate circuit was defined as the mKate2 output level in the presence versus the absence of the sponge (state [1,1] versus state [1,0] in Figure 2B). Ultimately, we chose a sponge architecture ***Sponge 7: H2A1p-EC1-10B<sub>ZRANBI</sub>-EC2-5B*** (Figure S2A) as the final ‘optimized sponge’ design, since it yielded the highest ON-OFF ratio for the AND gate circuit (~6-fold, Figure S2A).

In *Module 1*, we optimized the synthetic intronic pri-miRNA backbone in the self-inhibitory mKate2 transcript for enhanced miR1 production efficiency (Greber et al., 2008; Nissim et al., 2014; Xie et al., 2011). The absolute mKate2 signal in the OFF (no sponge, state [1,0]) and ON states (optimized sponge, state [1,1]) were both affected by the pri-miRNA designs we tested (Mv1-Mv3, Figure S3). Mv1 exhibited an OFF-ON shift from ~1400 to ~8400 Mean Fluorescence Intensity (MFI) (5.8-fold activation ratio), Mv2 from ~170 to ~500 MFI (3-fold activation), and Mv3 from ~380 to ~2600 MFI (6.8-fold activation). We selected the Mv3 architecture for further experimentation since it had low mKate2 level in OFF state, substantial absolute mKate2 levels in the ON state, and the highest fold-activation. However, we note that different designs could be more suitable for other targeting scenarios. For example, when using effector outputs with low potency, Mv1 could be chosen to achieve high absolute levels of expression in the ON state. Conversely, Mv2 could be suitable for expressing extremely potent outputs in which even low background output activity could be detrimental.

157

## 158 ***Synthetic Cancer-Specific Promoters***

159 To generate synthetic ovarian-cancer-specific promoters, we identified transcription fac-  
160 tors (TFs) that are overexpressed in ovarian cancer cells by comparing gene expression in prima-  
161 ry human ovarian tumors versus healthy controls, and their respective binding motifs, using pub-  
162 lically available databases (for more details, see Supplementary Information). In each synthetic  
163 promoter S(TF)p, multiple binding motifs for a single cancer-specific TF were encoded in tan-  
164 dem upstream to a synthetic minimal promoter derived from the major adenoviral late promoter  
165 (Figure 4A). This design approach resulted in compact promoters with evenly distributed and  
166 dense TF-BSs corresponding to a small number of TF families. For example, analysis of the 1 kb  
167 upstream of the transcriptional start site (TSS) of the native tumor-specific promoter H2A1p  
168 (Rogakou et al., 1998) revealed ~82 possible binding sites for 40 different TF families, with an  
169 mean of ~8 TF-BSs per 100bp. In comparison, the synthetic S(E2F1)p promoter, comprised of  
170 E2F1 binding sites, had only 44 possible binding sites for 7 different TF families, with a mean of  
171 ~16 TF-BSs per 100bp (Table S1; for more details on promoters analysis, see Supplementary  
172 Information).

173 We assayed the specificity and activity of natural and artificial promoters by infecting  
174 human OVCAR8 (OV8) ovarian cancer cells and normal primary cells, specifically primary  
175 adult human dermal fibroblasts (aHDF) and primary human ovarian epithelium (HOV). Several  
176 synthetic promoters, including S(E2F1)p and S(cMYC)p (comprised of E2F1 and cMYC binding  
177 sites, respectively), were highly active in OVCAR8 ovarian cancer cells but not in normal cells.  
178 These synthetic promoters exhibited greater activation ratios compared with known native tu-  
179 mor-specific promoters such as SSX1p (Gure et al., 1997) and H2A1p (Rogakou et al., 1998)  
180 (Figure 4B for selected promoters).

181 For example, SSX1p exhibited 9-fold activation in OVCAR8 compared to aHDF and 17-  
182 fold activation compared to HOV-epi (Figure 4B). H2A1p had 2-fold activation in OVCAR8  
183 compared to aHDF and 5.6-fold compared to HOV. The synthetic promoter S(E2F1)p had 224-  
184 fold induction in OVCAR8 versus aHDF and 570-fold activation in OVCAR8 compared to  
185 HOV, with absolute maximal expression levels comparable to the native promoters. S(cMYC)p  
186 exhibited 15-fold induction in OVCAR8 versus aHDF and 36-fold activation in OVCAR8 com-

pared to HOV. Since the maximal activity of S(cMYC)p was lower than S(E2F1)p in OVCAR8 cells, we selected S(cMYC)p to drive expression of *Module 1* and S(E2F1)p to drive the expression of *Module 2*. This was done so that the sponge could be expressed at a greater level than the miR1-encoding construct, which is important for achieving a high activation ratio with our circuit (Figure S2A).

### ***Multi-Output AND Gate for Combinatorial Immunomodulation***

To facilitate the expression of combinatorial immunomodulators from our circuit, we replaced mKate2 in *Module 1* with a synthetic transcription factor that activates the expression of downstream genes regulated by cognate synthetic promoters (Figure 5A). The artificial transcription factor implemented was the yeast GAL4 DNA-binding domain fused to the viral VP16 transcriptional activation domain (GAD), although other transcription factors could be used instead. Specifically, we used the synthetic promoter S(cMYC)p to express *Module 1* (**S(cMYC)p-GAD<sub>EX1</sub>-[miR1]<sub>cons</sub>-GAD<sub>EX2</sub>-11Pe**). *Module 1* encoded a self-inhibitory RNA transcript with miR1 as an intron within the GAD coding sequence followed by 11 tandem perfect match miR1 binding sites (11Pe) in the 3' UTR. In the *Module 2* vector, the synthetic promoter S(E2F1)p regulated the expression of the optimized sponge architecture (**Sponge 7: EC1-10B<sub>ZRANB1</sub>-EC2-5B**). Finally, we encoded an mKate2 output under the regulation of an artificial promoter targeted by GAD that contains GAL4-BSs upstream to a synthetic minimal late adenoviral promoter (GALp), namely *Module 3* (Figure 5A). We hypothesized that increasing the number of GAL4-BSs in the GALp would provide a convenient strategy for increasing output expression levels. We therefore built 3 different versions of GALp, either with 5, 8 or 14 tandem GAL4-BSs (G5p, G8p, and G14p, respectively). We further surmised that output levels in the OFF state could be lowered by adding miR1-BS(Pe) to the mKate2 output, thus allowing miR1 to reduce both GAD and mKate2 levels directly when the sponge is not active (Figure 5A). We therefore built 3 additional versions of the output vector in which a single perfect match miR1-BS (1Pe) was encoded in the 3' UTR of the output mKate2 transcript (G5-Pe, G8-Pe and G14-Pe, respectively). This design architecture enables convenient tuning of each output's expression levels based on the promoter and whether 1Pe was incorporated into the output transcript.

We first characterized the multi-output AND-gate architectures by modeling scenarios when neither (state [0,0]), only one (states [0,1] or [1,0]), or both cancer-specific promoters (state [1,1]) are active in a given cell type (Figure 5B). To do so, we encoded each module on separate lentiviruses and infected OVCAR8 cells with the corresponding *Module 3* architecture and either: (A) a negative control *Module 1* that expresses the non-specific transcription factor rtTA3 (*Module 1con*) and a negative control *Module 2* in which S(E2F1)p expresses ECFP without miR1-BS(B) (*Module 2con*) to model the scenario when neither cancer-specific promoters are active [0,0]; (B) *Module 1con* and *Module 2* to model the scenario when only S(E2F1)p is active [0,1]; (C) *Module 1* and *Module 2con* to model the scenario when only S(cMYC)p is active [1,0]; (D) *Module 1* and *Module 2* to model the scenario when both promoters are active [1,1].

The circuits expressed minimal mKate2 fluorescence in states [0,0] and [0,1]. In state [1,0], there was a low background mKate2 level that increased from 5 to 8 GAL4-BSs in the synthetic GALp and was attenuated with the presence of miR1-BS(Pe) in *Module 3* (Figure 5B). Only when both input constructs were present (state [1,1]) did we observe a significantly increased mKate2 output. Furthermore, the mKate2 output level could be enhanced by increasing the number of GAL4-BSs in the *Module 3* synthetic promoter from 5 to 8 GAL4-BSs. Although adding perfect match miR1 binding sites in the 3' UTR of the mKate2 transcript decreased the basal and maximal output levels, it also improved fold-activation (G5-Pe, G8-Pe, and G14-Pe versus G5, G8, and G14, respectively). The G8-Pe circuit exhibited negligible mKate2 levels in states [0,0] and [0,1], and high 8-fold mKate2 activation in state [1,1] over the minimal mKate2 expression in state [1,0], and was thus chosen for further use.

We next compared mKate2 expression from the G8-Pe circuit delivered via lentivirus in OVCAR8 cells versus normal cells, including primary aHDF, HOV, and human T cells. The circuit exhibited higher mKate2 expression in OVCAR8 versus aHDF and HOV in the [1,1] circuit configuration (4-fold and 71-fold, respectively, Figure 5C). We next determined the activity of the S(cMYC)p and S(E2F1)p promoters individually, as well as the activity of the G8-Pe circuit with S(cMYC)p and S(E2F1)p promoters as inputs, in primary human T cells. We observed that S(E2F1)p was significantly activated in primary human T cells. However, since S(cMYC)p was not active in these cells, the integrated output generated by the G8-Pe circuit was 30-fold lower

compared to the activity of S(E2F1)p on its own (Figure 5D & S4A). Furthermore, we tested the specificity of this design using additional cell lines, including non-tumorigenic human ovarian fibroblasts (HOF), non-tumorigenic human ovarian microvasculature epithelial cells (HOMECE), non-tumorigenic colonic epithelial cells (CCD-841-CoN), and non-tumorigenic mammary epithelial cells (MCF-10A and MCF-12A), as well as inducible pluripotent stem cells (iPSCs). The circuit achieved high specificity for OVCAR8 cells, with 10-fold to 800-fold higher circuit output in OVCAR8 cells versus these additional cell lines (Figure S4B). These data demonstrate the stringency of our circuit and the potential of our circuit design to enhance therapeutic specificity by reducing the probability of false-positive targeting compared to single promoter.

Finally, to demonstrate the modularity of our design, we examined whether the G8-Pe circuit could be adapted to target breast cancer cells by simple modification of the input promoters. For this purpose, we created two additional synthetic promoters, S(USF1)p and S(MAFK)p, that were designed to specifically target the MDA-MB-453 breast cancer cell line but not the MCF-10A non-tumorigenic mammary epithelial cell line. We compared the mKate2 outputs generated by each promoter individually versus the G8-Pe circuit in both cell lines. This new design generated a high output only in MDA-MB-453 cells, demonstrating the versatility of our circuit architecture and its ability to be adapted to a variety of different therapeutic scenarios and applications.

### ***STEs trigger T-cell-mediated cancer cell killing and IFN- $\gamma$ secretion***

Next, we sought to encode immunotherapies as the outputs of our synthetic cancer-specific circuits. An STE was constructed by fusing an scFv targeting human CD3 $\epsilon$  with an inert membrane anchor derived from the Duffy antigen/receptor for chemokines (DARC) of erythrocytes (von Nickisch-Rosenegk et al., 2012) (Figure 1B). We replaced mKate2 with STE as the output of the G8-Pe circuit and validated the therapeutic specificity of this circuit *in vitro*. We observed 20 to 118-fold higher STE expression on circuit-transduced OVCAR8 cells than on aHDF or HOV cells (Figure 6A). We also observed robust T-cell-mediated killing of circuit-transduced OVCAR8 cells, which was significantly higher than in aHDF or HOV cells (Figure 6B & Figure S4C-E). There was minimal T-cell-mediated killing of non-STE-expressing cells (Figure S4C-E), which could be caused by our experimental conditions, including MHC mis-

match between T cells and target cells as well as T-cell mediated killing with non-STE-based mechanisms (Kagi et al., 1994). In addition to direct tumor killing, robust IFN- $\gamma$  secretion by T cells is critical for strong therapeutic efficacy. We observed strong and specific IFN- $\gamma$  secretion by T cells only when they were co-cultured with circuit-transduced OVCAR8 cells (Figure 6C & Figure S4F), which was 20-28 fold higher than when T cells were co-cultured with circuit-transduced aHDF or HOV cells. We also observed minimal OVCAR8 killing and IFN- $\gamma$  secretion by T cells when *Module 2* was removed from the G8-Pe circuit (state [1,0]) to model the potential scenario in which one of the promoters exhibits some off-target activity (Figure 6A-C & Figure S4C-F).

We also performed a control experiment in which STE expression was regulated by the human Ubiquitin C (hUbC) promoter, which is constitutively active in OVCAR8, aHDF, and HOV cells. We examined the sensitivity of these cells to STE-mediated killing and their ability to trigger IFN- $\gamma$  production by T cells (Figure S4G-I). We found that while STE expression levels in OVCAR8 cells were ~3-fold higher than in aHDF and HOV cells, STE-mediated killing was comparable in aHDF and OVCAR8, and ~2-fold higher in HOV. In addition, all three STE-expressing cell lines triggered comparably strong IFN- $\gamma$  production by T cells. These results highlight the stringency of our AND gate, which mediates significantly higher OVCAR8 specificity over these other cell lines.

We next examined whether STE expression could trigger T-cell-mediated anti-tumor activity *in vivo*. OVCAR8 cells were transduced with lentiviruses encoding a doxycycline-inducible STE expression system and then injected *i.p.* into immunodeficient NSG mice on day 0. Since NSG mice lack T cells, human T cells were also periodically injected *i.p.* Specifically, STE expression was induced at day 14 followed by human T cell injections at day 16 and 31. In the absence of T cells, tumor growth was similar between the STE-induced and non-induced groups. STE expression led to a 6-fold decrease in tumor burden in mice treated with T cells compared to non-treated mice (Figure S4J-L), demonstrating that the anti-tumor activity of STEs was dependent on T cells. However, consistent with previous studies (Liao et al., 2003; Liu et al., 2011; Paul et al., 2002), STE expression on its own was unable to completely abrogate tumor growth, even when expressed in high levels in nearly all the tumor cells (Figure S4L).

## ***Tumor-specific expression of multiple immunotherapeutic outputs triggers effective T-cell-dependent tumor killing***

Since combination therapy has shown enhanced therapeutic efficacy over monotherapies (Lasek et al., 2014; Mahoney et al., 2015; Morrissey et al., 2016; Tugues et al., 2015) and STE expression alone was insufficient to achieve strong anti-tumor effects *in vivo*, we engineered our optimized cancer-specific gene circuit to generate multiple immunomodulators as outputs. To demonstrate the capability of the circuit to generate various types of commonly used immunomodulators, we implemented the SCIP combination, which includes a cell-surface antigen (STE) together with secreted chemokine (CCL21), cytokine (IL12), and checkpoint inhibitor (anti-PD1 antibody).

First, we transduced OVCAR8 cells with lentiviruses encoding the G8-Pe AND gate and the SCIP combination. We validated the selective co-production of STE, CCL21, IL12, and an anti-PD1 antibody from OVCAR8 cells, but not from aHDF or HOV cells, *in vitro* (Figure 6D-G). Next, we validated the functionality of our SCIP circuit with an *in vivo* model of human ovarian cancer. We engineered the G8-Pe circuit to produce a control output, STE only, or the SCIP combination in OVCAR8 cells. We then established *i.p.* disseminated ovarian cancers by injecting these OVCAR8 cells into the peritoneal cavity of NSG mice. This experimental setup was used to model the functionality of the circuit throughout the course of the treatment and its effects on circuit efficacy. For example, the activity of our input promoters could be altered in response to environmental signals or due to tumor heterogeneity, resulting in circuit inactivation and reduced efficacy.

In the absence of T cells, all tumors grew robustly (Figure S5A). When administered with T cells, tumor sizes in the control output (Control) and STE only groups were significantly larger than the STE+CCL21+IL12+anti-PD1 Ab (SCIP) combination, in which tumors were undetectable in most mice (Figure 7A & S5A-B). Significantly prolonged mice survival was also observed in the SCIP group (Figure 7B). Thus, combinatorial immunotherapies expressed from within tumor cells can mediate strong anti-tumor effects.

Next, we sought to confirm that the SCIP-expressing circuit could mediate robust efficacy even when it was only introduced into a small fraction of tumor cells. This experiment was used to model a common problem with tumor-targeting therapies in which the therapeutic circuit

is activated only in a fraction of the tumor. For example, this phenomenon can be mediated by modulation of gene expression, cellular heterogeneity within tumors, or partial circuit delivery. We mixed wild-type OVCAR8 cells with OVCAR8 cells containing the SCIP-expressing circuit in defined ratios. Even when only 15% or 30% of the overall tumor was composed of SCIP-expressing OVCAR8 cells, significant tumor reduction and survival was still achieved, only in the presence of T cells (Figure 7C-D & Figure S6A-B). This data suggests that immunomodulatory gene circuits may be able to mediate strong anti-tumor effects despite incomplete delivery in future applications.

Finally, we directly tested the efficacy of our SCIP circuit within *in vivo* delivery settings. To minimize the total number of viruses required to encode the entire SCIP circuit and thus simplify the delivery process, we combined the CCL21 and IL12 output modules into a single lentiviral construct by encoding both outputs, separated by a P2A peptide (Szymczak et al., 2004), under the regulation of a single G8 output promoter. We similarly combined the anti-PD1 Ab heavy chain and light chain modules into a single lentivirus. Mice with intraperitoneally disseminated tumors were injected *i.p.* with either a control lentivirus mix that contained *Module 1*, *Module 2* and a negative control output or a therapeutic virus mix that contained *Module 1*, *Module 2* and the SCIP outputs. Human T cells were also periodically injected *i.p.* Under these settings, we observed significantly reduced tumor burden and enhanced survival in mice treated with the SCIP circuit versus the control (Figure 7E-F & Figure S7A-B). This data indicates that *in vivo* delivery of our immunomodulatory gene circuits has the potential to trigger anti-tumor effects, even when it is encoded on multiple vectors.

## Discussion

In this study, we present a proof-of-concept demonstration that versatile genetic circuits can be engineered for highly specific production of combinatorial immunomodulators from within cancer cells. This modular design strategy can be further adapted to target additional tumor types and optimized for clinical translation. For example, we have shown that the circuit can be readily modified to target breast cancer cells by replacing the ovarian-cancer specific input promoters with other synthetic promoters that are breast-cancer specific. Furthermore, we showed



that these circuits could be delivered *in vivo* to trigger robust anti-tumor responses and increased survival of treated mice.

However, the *in vivo* efficacy model we utilized has several drawbacks limiting our ability to address questions such as *in vivo* targeting specificity and safety concerns. In our tumor model, tumor cells are of human origin and all other normal tissues are of mouse origin, thus making it challenging to address targeting specificity. Furthermore, NSG mice injected with human T cells eventually develop life threatening graft-versus-host disease (GVHD) (Covassin et al., 2011; Schroeder and DiPersio, 2011), making it difficult to study safety concerns related to therapy in this model. To further advance this approach towards therapeutic applications, these issues must be addressed. First, design and testing of circuits will likely need to be performed in additional tumor samples and tumor models. For example, specificity and efficacy should be further optimized and confirmed using patient-derived cancer cells and a panel of normal tissues. The potential off-target activity of circuit components, such as miR1 and the miRNA sponge, should also be examined, for example via transcriptomics. Moreover, while our *in vitro* assays allow for testing of short-term specificity, future efforts should measure long-term specificity and side effects within *in vivo* settings. Second, additional *in vivo* cancer models that account for tumor heterogeneity should be used in efficacy assays, such as patient-derived xenografts (Morel et al., 2016). Third, we evaluated the anti-tumor efficacy of our combinatorial immunomodulators in NSG mice with supplemented human T cells, which does not capture the full immune response. Future work will be needed to optimize and characterize specific immunomodulatory combinations with high efficacy and safety in additional cancer models, including humanized mice or syngeneic mouse models with intact immune systems. Such systems may be able to model the efficacy and safety effects of our therapeutic approach on other arms of the immune system and on important phenomena such as epitope spreading (el-Shami et al., 1999). Mice in such systems do not develop GVHD and may enable us to address safety concerns related to the therapy. Fourth, the exact combination of immunomodulatory outputs will likely need to be optimized for different tumor types. Finally, improved delivery strategies will be needed to convey our immunomodulatory gene circuits into tumors. These genetically engineered circuits could be delivered into tumors using non-viral carriers, such as HPAE (Zhou et al., 2016), as well as oncolytic viruses, such as HSV-1 (Andtbacka et al., 2015; Zhang et al., 2013). Given that only 15% of tumor cells had to express the circuit to achieve robust anti-tumor responses in our model

(Figure 7C-D & Figure S6) and that our circuit could mediate anti-tumor effects when delivered *in vivo* by multiple lentiviruses (Figure 7E-F & Figure S7), we hypothesize that delivery efficiencies will not need to be perfect to achieve a therapeutic effect. However, we note that delivery requirements will likely vary in other tumor models.

Furthermore, it will be useful to test whether our approach can be used in combination with other therapeutic strategies to enhance efficacy. For example, our approach may be useful in improving therapy with Tumor-Infiltrating Lymphocytes (TIL) and CAR-T cells by tumor-specific secretion of immunomodulators that attract immune cells to the tumor site and activate them while disrupting the immunosuppressive microenvironment. For example, TILs and CAR-T cells engineered to secrete IL12 exhibited stronger efficacy than non-IL12 secreting counterparts (Koneru et al., 2015; Pegram et al., 2012; Zhang et al., 2015). However, IL12-secreting TILs mediated significant systemic toxicity in a clinical trial (Zhang et al., 2015), probably since T cells can patrol throughout the body and thus produce IL12 systemically. Thus, it may be safer to use non-IL12-secreting TILs or CAR-T cells together with circuit-triggered IL12 secretion from within tumors.

Additionally, recent studies have shown that many tumors express immunogenic neoantigens that can be targeted by the host immune system (Schumacher and Schreiber, 2015). We speculate that using our strategy to trigger tumor killing in combination with neoantigen-based immunotherapies could be a fruitful approach to investigate (Carreno et al., 2015; Cohen et al., 2015; Gros et al., 2016; Gubin et al., 2015; Schumacher and Schreiber, 2015), for example, by triggering robust T-cell-mediated killing of cancer cells and the release of such neoantigens. Furthermore, secreted immunomodulators could disrupt immunosuppressive tumor microenvironments to enhance neoantigen presentation by antigen-presenting cells and further improve anti-tumor immune responses.

Since our approach enables tumor-specific secretion of defined combinations of immunomodulators, it could be a useful framework to study the immunological mechanisms that underlie tumor biology. Moreover, synthetic gene circuits have been shown to have the potential to treat immunological disorders by sensing extracellular disease markers (Schukur et al., 2015). Similarly, our approach for sensing internal cell states with multiple artificial promoters could be adapted to treat other complex diseases that require highly specific and multifactorial program-

425 ming of immunological functions with simple modifications to the synthetic promoter inputs and  
426 immunomodulatory outputs.

427         In summary, modulating the immune system is a promising approach to treating complex  
428 diseases. However, multiple disease-mediated mechanisms can limit the effectiveness of mono-  
429 therapies (Mahoney et al., 2015; Morrissey et al., 2016). Combinatorial immunomodulators can  
430 be used to overcome this difficulty, but given the broad effects of the immune system on human  
431 physiology, it will be important to constrain the activity of immunomodulators to specific disease  
432 compartments to avoid undesirable side effects and maximize efficacy (Boutros et al., 2016;  
433 Carson et al., 2000). Thus, we envision that synthetic gene circuit immunotherapies that are high-  
434 ly specific, tunable, and amenable to combinatorial effector expression will provide powerful  
435 strategies for engineering the immune system to understand and treat disease.

## Methods

### *Plasmid construction*

The various circuit modules, synthetic promoters, and immunomodulatory constructs were built using conventional restriction enzyme cloning and Gibson assembly. Plasmids compositions used in each experiment are detailed in supplemental file “Plasmids by figures.pdf”. All DNA sequences used in this study are detailed in GenBank format in the single text file “All sequences.docx”. Additionally, individual GenBank and SnapGene sequence files for the plasmids in this study can be downloaded from a public Dropbox folder using the link below:

<https://www.dropbox.com/sh/wbq2y3lx87yzppe/AAAvFM7g6b1K35Ay1zSreoGDa?dl=0>

### *Cell culture and cell lines*

HEK-293T, adult Human Dermal Fibroblast (aHDF), MDA-MB-453, MCF-10A, MCF-12A, and CCD-841-CoN cells were obtained from the American Type Culture Collection, Rockville, MD (HEK293T, Catalog #CRL-3216; aHDF, Catalog #PCS-201-012; MDA-MB-453, Catalog #HTB-131; MCF-10A, Catalog #CRL-10317; MCF-12A, Catalog #CRL-10782; CCD-841-CoN, Catalog #CRL-1790). Ovarian carcinoma cell line 8 (OVCAR8) engineered to stably express firefly luciferase (OVCAR8-Luc) was a gift from S. N. Bhatia (Massachusetts Institute of Technology, Cambridge, MA). Primary human ovarian epithelial cells (HOV), primary human ovarian fibroblasts (HOF), and primary human ovarian microvasculature endothelial cells (HOMECE) were obtained from ScienCell Research Laboratories, Carlsbad, CA (HOV, Catalog #7310; HOF, Catalog #7330; HOMECE, Catalog #7300). Inducible pluripotent stem cell (iPSC) was a gift from R. Weiss (Massachusetts Institute of Technology). HEK-293T, OVCAR8-Luc, aHDF, and MDA-MB-453 cells were cultured in DMEM (Life Technologies, Carlsbad, CA) supplemented with 10% fetal bovine serum (FBS; VWR, Radnor, PA; Catalog #95042-108), 1% Non-Essential Amino Acids (MEM/NEAA; Hyclone; Catalog #16777-186), and 1% Pen/Strep (Life Technologies Catalog #15140-122) at 37 °C with 5% CO<sub>2</sub>. HOV cells were cultured in Ovarian Epithelial Cell Medium (ScienCell Research Laboratories Catalog #7311) supplemented with Pen/Strep (ScienCell Research Laboratories Catalog #0503), Ovarian Epithelial Cell Growth Supplement (ScienCell Research Laboratories Catalog #7352) and grown on a poly-L-lysine (Sigma-Aldrich, St. Louis, MO; Catalog #P4707-50ML) coated-plate. HOF cells were cul-

468 tured in Fibroblast Medium (ScienCell Research Laboratories Catalog #2301) supplemented with  
469 Pen/Strep (ScienCell Research Laboratories Catalog #0503), Fetal Bovine Serum (ScienCell Re-  
470 search Laboratories Catalog #0010), Fibroblast Growth Supplement (ScienCell Re-search Labor-  
471 atories Catalog #2352) and grown on a poly-L-lysine (Sigma-Aldrich Catalog #P4707-50ML)  
472 coated-plate. HOME C cells were cultured in Endothelial Cell Medium (ScienCell Research La-  
473 boratories Catalog #1001) supplemented with Pen/Strep (ScienCell Research Laboratories Cata-  
474 log #0503), Fetal Bovine Serum (ScienCell Research Laboratories Catalog #0025), Endothelial  
475 Cell Growth Supplement (ScienCell Research Laboratories Catalog #1052) and grown on a Fi-  
476 bronectin (Sigma-Aldrich Catalog #F1141-2MG) coated-plate. MCF-10A and MCF-12A cells  
477 were cultured in MEGM BulletKit (Lonza, Walkersville, MD; Catalog #CC-3151 & CC-4136).  
478 All cell lines were banked directly after being purchased from vendors and used at low passage  
479 numbers. Cell lines were tested negative for mycoplasma contamination with IMPACT PCR by  
480 the Division of Comparative Medicine Diagnostic Lab at MIT.

481 Human PBMCs were obtained from leukoreduction collar (Brigham and Women's hospi-  
482 tal Crimson Core Laboratory, Boston, MA) with gradient centrifugation. To culture and expand  
483 human T cells, human PBMCs were stimulated with 40 ng/mL of anti-human CD3 antibody  
484 (clone: OKT3; BioLegend, San Diego, CA ;Catalog #317304) for 3 days in RPMI 1640 (Invitro-  
485 gen, Carlsbad, CA; Catalog #11875119), supplemented with 10% heat-inactivated FBS, 10 mM  
486 HEPES (Life Technologies Catalog #15630080), 0.1 mM non-essential amino acids, 1 mM sodi-  
487 um pyruvate (Life Technologies Catalog #11360-070), 1% Pen/Strep, 50  $\mu$ M 2-Mercaptoethanol  
488 (Sigma-Aldrich Catalog #M3148-25ML ), and 50 IU/mL recombinant human IL-2 (NCI, Freder-  
489 ick, MD).

### 491 ***Transfection for AND gate optimization***

492 To optimize the AND gate circuit in Figure 2-3 and Figure S1-3, we tested different  
493 combinations of two plasmids: *Module 1* variants expressed an auto-inhibitory mKate2 RNA  
494 transcript regulated by synthetic miRNA (miR1) and *Module 2* variants expressed sponges for  
495 miR1 within an ECFP transcript, where ECFP enables us to assess sponge expression. In brief,  
496 12  $\mu$ l of FuGENE HD transfection reagent (Promega, Madison, WI; Catalog #E2311) mixed with  
497 100  $\mu$ l of OptiMEM medium (Life Technologies Catalog #31985) was added to the mixture of  
498 two plasmids (1  $\mu$ g each). During 20 minutes incubation of FuGENE HD/DNA complexes at

room temperature, HEK-293T suspension cells were prepared and diluted to  $1.2 \times 10^6$  cells/ml in culture medium. 0.5 ml of diluted cells ( $0.6 \times 10^6$  cells) were added to each FuGENE HD/DNA complex tube, mixed well, and after 5 min incubation at room temperature transferred to a designated well in 6-well plate containing 2 ml cell culture medium, followed by incubation at 37 °C with 5% CO<sub>2</sub>. Transfected cells were prepared for FACS analysis at 48-hour post-transfection.

### ***Lentivirus production and transduction***

Lentiviruses were produced in HEK-293T cells using co-transfection in 6-well plate format. In brief, 12 µl of FuGENE HD was mixed with 100 µl of OptiMEM medium and was added to a mixture of 3 plasmids: 0.5 µg of pCMV-VSV-G vector, 0.5 µg of lentiviral packaging psPAX2 vector, and 1 µg of lentiviral expression vector. During 20 minutes incubation of FuGENE HD/DNA complexes at room temperature, HEK-293T suspension cells were prepared and diluted to  $3.6 \times 10^6$  cells/ml in cell culture medium. 0.5 ml of diluted cells ( $1.8 \times 10^6$  cells) were added to each FuGENE HD/DNA complex tube, mixed well, and incubated for 5 min at room temperature before being added to a designated well in 6-well plate containing 1 ml cell culture medium, followed by incubation at 37°C with 5% CO<sub>2</sub>. Media of transfected cells were replaced with 2.5 ml fresh culture media 18 hours post transfection. Supernatant containing newly produced viruses was collected at 48-hour post-transfection, and filtered through a 0.45 µm syringe filter (Pall Corporation, Ann Arbor, MI; Catalog #4614).

For testing of synthetic promoters (Figure 4A-B), 1:9 dilutions of filtered viral supernatants were prepared and 3 ml of each individual virus was used to infect  $2.5 \times 10^5$  OVCAR8-Luc, aHDF or HOV cells in the presence of 8 µg/ml polybrene (Sigma) overnight. For optimizing and testing the GAD-expressing gate (Figure 5A-E), we transduced three viruses encoding *Module 1*, *Module 2*, and *Module 3*. Each virus was diluted 1:3 and we used 3 ml of the pooled viruses to infect  $2.5 \times 10^5$  target cells in the presence of 8 µg/ml polybrene (Sigma) overnight. Cell culture medium was replaced the next day after infection and cells were cultured for at least one week prior to FACS analysis or cytotoxicity assay. For creating cell lines bearing circuits expressing multiple outputs (Figure 6D-G, Figure 7), two rounds of lentiviral infection were performed. The viruses for the first round consisted of *Module 1*, *Module 2*, and an output construct expressing STE. The viruses for the second round consisted of output constructs expressing all other outputs.

### ***Flow cytometry***

For characterizing fluorescent protein expression, cells were resuspended with DMEM and analyzed by a LSRII Fortessa cytometer (BD Biosciences, San Jose, CA). To characterize STE display and expression level on cell surfaces, various cell lines were stained with phycoerythrin labeled anti-HA tag Ab (Miltenyi Biotec; catalog #130-092-257). Data analysis was performed by FlowJo software (TreeStar Inc, Ashland, OR).

### ***T cell-mediated cell lysis in vitro***

T cell-mediated cell lysis was measured by LDH release assay with CytoTox 96<sup>®</sup> Non-Radioactive Cytotoxicity Assay Kit (Promega, Madison, WI; catalog #G1780). Human T cells were incubated with circuit-expressing target cells at a effector to target ratio (E:T ratio) of 20:1 ( $6 \times 10^5$ : $3 \times 10^4$ ) in duplicate wells in 96 well flat-bottom plates. T cells and target cells were also plated alone to determine spontaneous LDH release from T cells (“effector spontaneous”) and from target cells (“target spontaneous”). A set of target cells were also plated and lysed with lysis buffer for determining maximal LDH release (“target maximum”). 8.5 hours later, cell-free culture supernatant was harvested and LDH release was determined following the manufacturer’s protocol. T cell-mediated lysis was calculated as: percentage of T cell-mediated lysis = [(experimental O.D. value - effector spontaneous O.D. value - target spontaneous O.D. value) / (target maximum O.D. value - target spontaneous O.D. value)] x 100. Media O.D. values were subtracted from all samples before calculation. STE mediated lysis was calculated as: T cell mediated lysis of STE expressing cells - T cell mediated lysis of non-STE expressing cells. The results of each experiment represent three biological replicates.

### ***IFN- $\gamma$ production by T cells***

Human T cells were co-cultured with tumor cells at an E:T ratio = 20:1 ( $6 \times 10^5$ : $3 \times 10^4$ ) in duplicate wells in 96 well flat-bottom plates. Cell-free medium was collected after 24h and IFN- $\gamma$  concentration determined by Human IFN- $\gamma$  DuoSet ELISA (R&D systems, Minneapolis, MN; catalog #DY285).

***Multiple-output circuit triggers STE, CCL21, IL12, and anti-PD1 Ab production specifically by OVCAR8 cells***

To validate STE, CCL21, IL12, and anti-PD1 Ab production by OVCAR8 cells but not by normal cells (Figure 6D-G),  $2 \times 10^5$  OVCAR8-Luc, HOV, or aHDF cells transduced with the SCIP-expressing circuit were plated in 6-well plates and cell-free medium was collected after 72h. Displayed STE on cell surfaces was measured via staining with phycoerythrin labeled anti-HA tag Ab (Miltenyi Biotec) or phycoerythrin labeled anti-His tag Ab (Miltenyi Biotec) and quantified by flow cytometry analysis. CCL21 concentration was determined by Human CCL21/6Ckine DuoSet ELISA (R&D systems; catalog #DY366). IL-12 concentration was determined by Human IL-12 p70 DuoSet ELISA (R&D systems; catalog #DY1270), and anti-PD1 Ab production was validated by a competitive staining approach. The competitive staining was done by incubating cell-free medium (circuit-conditioned or control medium) with activated human T cells for 30 minutes, then followed by staining with anti-human CD279 (PD-1) Ab [clone: EH12.2H7; BioLegend; catalog #329920]. The percentage signal reduction was calculated by the following equation:  $(1 - \text{PD1 staining MFI of T cells incubated with circuit-conditioned medium} / \text{PD1 staining MFI of T cells incubated with control medium}) * 100\%$ .

***Mice***

Female NSG mice (NOD.Cg-*Prkdc*<sup>scid</sup> *Il2rg*<sup>tm1Wjl</sup>/SzJ; Stock No: 005557) were purchased from the Jackson Laboratory (Bar Harbor, ME). Mice were used in experiments at the age of 8-13 weeks old. All experiments were conducted at the Koch Institute Animal Facility under a protocol approved by MIT's Committee on Animal Care.

***In vivo experiments validating circuit therapeutic efficacy***

For *in vivo* experiments, animals were randomly assigned to each experimental group. No specific inclusion/exclusion criteria were used for animal studies. Investigators were not blinded to animal groups. Four to five mice were used in each experimental group. To validate STE therapeutic efficacy on ovarian cancer, OVCAR8-Luc cells expressing doxycycline (Dox)-inducible STE ( $5 \times 10^5$  cells) were injected intraperitoneally (i.p.) into NSG mice on day 0, and STE expression were induced by Dox [0.2mg/mL Dox + 2% Sucrose (Sigma-Aldrich; catalog #S3929-1KG) in drinking water] at day 14. Activated human T cells ( $10^7$  cells) were injected at day 16 and 31.



For measuring tumor burden, mice were injected with 30mg of VivoGlo™ Luciferin, In Vivo Grade (Promega; catalog #P1043) 10 minutes prior to bioluminescence imaging (IVIS spectrum optical imaging system, Xenogen, Alameda, CA).

To measure the efficacy of different therapeutic output combinations on ovarian cancer, OVCAR8-Luc cells ( $5 \times 10^5$  cells) engineered to express various outputs were injected i.p. into NSG mice on day 0. Activated human T cells ( $10^7$  cells) were injected at day 7, 14, 21 and 28. Tumor burden was monitored by IVIS imaging using the protocol described above. To measure survival, mice were euthanized when they developed signs of distress, such as ruffled fur, poor body posture, distended abdomen, and jaundice.

To identify the minimal percentage of tumor cells needed to be transduced with the SCIP-expressing circuit to mediate robust therapeutic efficacy, OVCAR8-Luc cells engineered with the SCIP-expressing circuit were mixed with wild-type OVCAR8-Luc cells at various ratios (15% to 85%; 30% to 70%).  $5 \times 10^5$  mixed OVCAR8-Luc cells were injected i.p. into NSG mice on day 0. Activated human T cells ( $10^7$  cells) were injected at day 9, 16, and 23. Tumor burden was monitored by IVIS imaging using the protocol described above. We used the criteria described above to measure survival.

To deliver the SCIP circuit with lentivirus *in vivo*, lentiviruses for each circuit component (*Module 1*, *Module 2*, STE, CCL21+IL12, and anti-PD1 Ab, see Figure 7E for more details) were produced as described above. For the SCIP therapy group, 10 mL of viruses for each of the five circuit components were collected and concentrated 15-fold using Amicon 100K MW cutoff ultrafiltration columns (Millipore, catalog #UFC910024). For the control group, 10 mL of viruses for *Module 1*, 10 mL of viruses for *Module 2*, and 30 mL of viruses encoding the control output (rtTA3) was collected and concentrated. After concentration, viruses were pooled and a p24 ELISA kit (Advanced Bioscience Laboratories, catalog #5421) was used to determine the viral titer. The pooled viruses had titers of  $\sim 7 \times 10^{10}$  viral particles/mL. Polybrene was added to the viruses to reach a final concentration of 16  $\mu\text{g/mL}$ . 600  $\mu\text{L}$  of viral supernatant was injected into mice intraperitoneally.

## Acknowledgements

LN dedicates this work to Zmira Nissim. LN thanks Yaakov Nissim, Aviva Yitzhak and Ovad Nissim for their invaluable support. We thank Ramez Daniel for discussion and Karen Weisinger for editing the manuscript. We thank the staffs of Division of Comparative Medicine at Koch Institute for Integrative Cancer Research at Massachusetts Institute of Technology for helping with animal experiments. We thank Swanson Biotechnology Center at Koch Institute for assisting with animal imaging. This work was supported by the National Institutes of Health, the Department of Defense, the Defense Advanced Research Projects Agency, and the Koch Institute for Integrative Cancer Research.

## Author Contributions

LN, MW, and TKL conceived and designed the study. LN, MW, EP and AN performed experiments and analyzed data. HIS and PAS performed the miRNA backbone optimization. DS, CW, and YT performed computational analysis and bioinformatics framework for synthetic promoters design. LN, MW, EP, AN, HIS, DS, CW, YT, PAL and TKL wrote the paper. All authors discussed the results and reviewed the manuscript.

## Competing Financial Interests

LN, MW, and TKL have filed a patent application on this work.

## References

- Andtbacka, R.H., Kaufman, H.L., Collichio, F., Amatruda, T., Senzer, N., Chesney, J., Delman, K.A., Spitler, L.E., Puzanov, I., Agarwala, S.S., *et al.* (2015). Talimogene Laherparepvec Improves Durable Response Rate in Patients With Advanced Melanoma. *J Clin Oncol* 33, 2780-2788.
- Auyeung, V.C., Ulitsky, I., McGeary, S.E., and Bartel, D.P. (2013). Beyond Secondary Structure: Primary-Sequence Determinants License Pri-miRNA Hairpins for Processing. *Cell* 152, 844-858.
- Bacchus, W., Aubel, D., and Fussenegger, M. (2013). Biomedically relevant circuit-design strategies in mammalian synthetic biology. *Molecular Systems Biology* 9, 691.
- Bell, J., and McFadden, G. (2014). Viruses for tumor therapy. *Cell Host Microbe* 15, 260-265.
- Bojar, D., and Fussenegger, M. (2016). The best of both worlds: reaping the benefits from mammalian and bacterial therapeutic circuits. *Curr Opin Chem Biol* 34, 11-19.

652 Boutros, C., Tarhini, A., Routier, E., Lambotte, O., Ladurie, F.L., Carbonnel, F., Izzeddine, H.,  
 653 Marabelle, A., Champiat, S., Berdelou, A., *et al.* (2016). Safety profiles of anti-CTLA-4 and  
 654 anti-PD-1 antibodies alone and in combination. *Nat Rev Clin Oncol* 13, 473-486.  
 655 Carreno, B.M., Magrini, V., Becker-Hapak, M., Kaabinejadian, S., Hundal, J., Petti, A.A., Ly,  
 656 A., Lie, W.R., Hildebrand, W.H., Mardis, E.R., *et al.* (2015). Cancer immunotherapy. A  
 657 dendritic cell vaccine increases the breadth and diversity of melanoma neoantigen-specific T  
 658 cells. *Science* 348, 803-808.  
 659 Carson, W.E., Dierksheide, J.E., Jabbour, S., Anghelina, M., Bouchard, P., Ku, G., Yu, H.,  
 660 Baumann, H., Shah, M.H., Cooper, M.A., *et al.* (2000). Coadministration of interleukin-18 and  
 661 interleukin-12 induces a fatal inflammatory response in mice: critical role of natural killer cell  
 662 interferon-gamma production and STAT-mediated signal transduction. *Blood* 96, 1465-1473.  
 663 Chmielewski, M., Hombach, A.A., and Abken, H. (2014). Of CARs and TRUCKs: chimeric  
 664 antigen receptor (CAR) T cells engineered with an inducible cytokine to modulate the tumor  
 665 stroma. *Immunol Rev* 257, 83-90.  
 666 Cohen, C.J., Gartner, J.J., Horovitz-Fried, M., Shamalov, K., Trebska-McGowan, K.,  
 667 Bliskovsky, V.V., Parkhurst, M.R., Ankri, C., Prickett, T.D., Crystal, J.S., *et al.* (2015). Isolation  
 668 of neoantigen-specific T cells from tumor and peripheral lymphocytes. *J Clin Invest* 125, 3981-  
 669 3991.  
 670 Covassin, L., Laning, J., Abdi, R., Langevin, D.L., Phillips, N.E., Shultz, L.D., and Brehm, M.A.  
 671 (2011). Human peripheral blood CD4 T cell-engrafted non-obese diabetic-scid IL2rgamma(null)  
 672 H2-Ab1 (tm1Gru) Tg (human leucocyte antigen D-related 4) mice: a mouse model of human  
 673 allogeneic graft-versus-host disease. *Clin Exp Immunol* 166, 269-280.  
 674 Ebert, M.S., and Sharp, P.A. (2010). MicroRNA sponges: Progress and possibilities. *Rna* 16,  
 675 2043-2050.  
 676 el-Shami, K., Tirosh, B., Bar-Haim, E., Carmon, L., Vadai, E., Fridkin, M., Feldman, M., and  
 677 Eisenbach, L. (1999). MHC class I-restricted epitope spreading in the context of tumor rejection  
 678 following vaccination with a single immunodominant CTL epitope. *Eur J Immunol* 29, 3295-  
 679 3301.  
 680 Fellmann, C., Hoffmann, T., Sridhar, V., Hopfgartner, B., Muhar, M., Roth, M., Lai, D.Y.,  
 681 Barbosa, I.A.M., Kwon, J.S., Guan, Y.Z., *et al.* (2013). An Optimized microRNA Backbone for  
 682 Effective Single-Copy RNAi. *Cell Reports* 5, 1704-1713.  
 683 Fenno, L.E., Mattis, J., Ramakrishnan, C., Hyun, M., Lee, S.Y., He, M., Tucciarone, J.,  
 684 Selimbeyoglu, A., Berndt, A., Grosenick, L., *et al.* (2014). Targeting cells with single vectors  
 685 using multiple-feature Boolean logic. *Nat Methods* 11, 763-772.  
 686 Greber, D., El-Baba, M.D., and Fussenegger, M. (2008). Intronic encoded siRNAs improve  
 687 dynamic range of mammalian gene regulation systems and toggle switch. *Nucleic Acids*  
 688 *Research* 36, e101.  
 689 Gros, A., Parkhurst, M.R., Tran, E., Pasetto, A., Robbins, P.F., Ilyas, S., Prickett, T.D., Gartner,  
 690 J.J., Crystal, J.S., Roberts, I.M., *et al.* (2016). Prospective identification of neoantigen-specific  
 691 lymphocytes in the peripheral blood of melanoma patients. *Nat Med* 22, 433-438.  
 692 Gubin, M.M., Artyomov, M.N., Mardis, E.R., and Schreiber, R.D. (2015). Tumor neoantigens:  
 693 building a framework for personalized cancer immunotherapy. *J Clin Invest* 125, 3413-3421.  
 694 Gure, A.O., Tureci, O., Sahin, U., Tsang, S., Scanlan, M.J., Jager, E., Knuth, A., Pfreundschuh,  
 695 M., Old, L.J., and Chen, Y.T. (1997). SSX: A multigene family with several members  
 696 transcribed in normal testis and human cancer. *International Journal of Cancer* 72, 965-971.

697 Haraguchi, T., Ozaki, Y., and Iba, H. (2009). Vectors expressing efficient RNA decoys achieve  
 698 the long-term suppression of specific microRNA activity in mammalian cells. *Nucleic Acids Res*  
 699 37.  
 700 Hassan, R., and Ho, M. (2008). Mesothelin targeted cancer immunotherapy. *Eur J Cancer* 44, 46-  
 701 53.  
 702 Kagi, D., Vignaux, F., Ledermann, B., Burki, K., Depraetere, V., Nagata, S., Hengartner, H., and  
 703 Golstein, P. (1994). Fas and perforin pathways as major mechanisms of T cell-mediated  
 704 cytotoxicity. *Science* 265, 528-530.  
 705 Kershaw, M.H., Westwood, J.A., Slaney, C.Y., and Darcy, P.K. (2014). Clinical application of  
 706 genetically modified T cells in cancer therapy. *Clin Transl Immunology* 3, e16.  
 707 Kertesz, M., Iovino, N., Unnerstall, U., Gaul, U., and Segal, E. (2007). The role of site  
 708 accessibility in microRNA target recognition. *Nature Genetics* 39, 1278-1284.  
 709 Klebanoff, C.A., Rosenberg, S.A., and Restifo, N.P. (2016). Prospects for gene-engineered T cell  
 710 immunotherapy for solid cancers. *Nat Med* 22, 26-36.  
 711 Koneru, M., Purdon, T.J., Spriggs, D., Koneru, S., and Brentjens, R.J. (2015). IL-12 secreting  
 712 tumor-targeted chimeric antigen receptor T cells eradicate ovarian tumors in vivo.  
 713 *Oncoimmunology* 4, e994446.  
 714 Kotula, J.W., Kerns, S.J., Shaket, L.A., Siraj, L., Collins, J.J., Way, J.C., and Silver, P.A. (2014).  
 715 Programmable bacteria detect and record an environmental signal in the mammalian gut.  
 716 *Proceedings of the National Academy of Sciences of the United States of America* 111, 4838-  
 717 4843.  
 718 Lasek, W., Zagozdzon, R., and Jakobisiak, M. (2014). Interleukin 12: still a promising candidate  
 719 for tumor immunotherapy? *Cancer Immunol Immunother* 63, 419-435.  
 720 Lee, C.H., Chiang, Y.H., Chang, S.E., Chong, C.L., Cheng, B.M., and Roffler, S.R. (2009).  
 721 Tumor-localized ligation of CD3 and CD28 with systemic regulatory T-cell depletion induces  
 722 potent innate and adaptive antitumor responses. *Clin Cancer Res* 15, 2756-2766.  
 723 Lengyel, E., Burdette, J.E., Kenny, H.A., Matei, D., Pilrose, J., Haluska, P., Nephew, K.P.,  
 724 Hales, D.B., and Stack, M.S. (2014). Epithelial ovarian cancer experimental models. *Oncogene*  
 725 33, 3619-3633.  
 726 Leonard, J.P., Sherman, M.L., Fisher, G.L., Buchanan, L.J., Larsen, G., Atkins, M.B., Sosman,  
 727 J.A., Dutcher, J.P., Vogelzang, N.J., and Ryan, J.L. (1997). Effects of single-dose interleukin-12  
 728 exposure on interleukin-12-associated toxicity and interferon-gamma production. *Blood* 90,  
 729 2541-2548.  
 730 Liao, K.W., Chen, B.M., Liu, T.B., Tzou, S.C., Lin, Y.M., Lin, K.F., Su, C.I., and Roffler, S.R.  
 731 (2003). Stable expression of chimeric anti-CD3 receptors on mammalian cells for stimulation of  
 732 antitumor immunity. *Cancer Gene Ther* 10, 779-790.  
 733 Liao, K.W., Lo, Y.C., and Roffler, S.R. (2000). Activation of lymphocytes by anti-CD3 single-  
 734 chain antibody dimers expressed on the plasma membrane of tumor cells. *Gene Ther* 7, 339-347.  
 735 Lin, Y., Sharma, S., and John, M.S. (2014). CCL21 Cancer Immunotherapy. *Cancers (Basel)* 6,  
 736 1098-1110.  
 737 Liu, Y., Tuve, S., Persson, J., Beyer, I., Yumul, R., Li, Z.Y., Tragoolpua, K., Hellstrom, K.E.,  
 738 Roffler, S., and Lieber, A. (2011). Adenovirus-mediated intratumoral expression of  
 739 immunostimulatory proteins in combination with systemic Treg inactivation induces tumor-  
 740 destructive immune responses in mouse models. *Cancer Gene Ther* 18, 407-418.

741 Liu, Y.C., Zeng, Y.Y., Liu, L., Zhuang, C.L., Fu, X., Huang, W.R., and Cai, Z.M. (2014).  
 742 Synthesizing AND gate genetic circuits based on CRISPR-Cas9 for identification of bladder  
 743 cancer cells. *Nature Communications* 5.  
 744 Mahoney, K.M., Rennert, P.D., and Freeman, G.J. (2015). Combination cancer immunotherapy  
 745 and new immunomodulatory targets. *Nat Rev Drug Discov* 14, 561-584.  
 746 Maude, S.L., Frey, N., Shaw, P.A., Aplenc, R., Barrett, D.M., Bunin, N.J., Chew, A., Gonzalez,  
 747 V.E., Zheng, Z., Lacey, S.F., *et al.* (2014). Chimeric antigen receptor T cells for sustained  
 748 remissions in leukemia. *N Engl J Med* 371, 1507-1517.  
 749 Morel, M., Shtrahman, R., Rotter, V., Nissim, L., and Bar-Ziv, R.H. (2016). Cellular  
 750 heterogeneity mediates inherent sensitivity-specificity tradeoff in cancer targeting by synthetic  
 751 circuits. *Proc Natl Acad Sci U S A* 113, 8133-8138.  
 752 Morgan, R.A., Yang, J.C., Kitano, M., Dudley, M.E., Laurencot, C.M., and Rosenberg, S.A.  
 753 (2010). Case report of a serious adverse event following the administration of T cells transduced  
 754 with a chimeric antigen receptor recognizing ERBB2. *Mol Ther* 18, 843-851.  
 755 Morrissey, K.M., Yuraszek, T.M., Li, C.C., Zhang, Y., and Kasichayanula, S. (2016).  
 756 Immunotherapy and Novel Combinations in Oncology: Current Landscape, Challenges, and  
 757 Opportunities. *Clin Transl Sci* 9, 89-104.  
 758 Neri, D., and Sondel, P.M. (2016). Immunocytokines for cancer treatment: past, present and  
 759 future. *Current Opinion in Immunology* 40, 96-102.  
 760 Newick, K., Moon, E., and Albelda, S.M. (2016). Chimeric antigen receptor T-cell therapy for  
 761 solid tumors. *Mol Ther Oncolytics* 3, 16006.  
 762 Nissim, L., and Bar-Ziv, R.H. (2010). A tunable dual-promoter integrator for targeting of cancer  
 763 cells. *Molecular Systems Biology* 6.  
 764 Nissim, L., Perli, S.D., Fridkin, A., Perez-Pinera, P., and Lu, T.K. (2014). Multiplexed and  
 765 programmable regulation of gene networks with an integrated RNA and CRISPR/Cas toolkit in  
 766 human cells. *Mol Cell* 54, 698-710.  
 767 Pardee, K., Green, A.A., Takahashi, M.K., Braff, D., Lambert, G., Lee, J.W., Ferrante, T., Ma,  
 768 D., Donghia, N., Fan, M., *et al.* (2016). Rapid, Low-Cost Detection of Zika Virus Using  
 769 Programmable Biomolecular Components. *Cell* 165, 1255-1266.  
 770 Paul, S., Regulier, E., Rooke, R., Stoeckel, F., Geist, M., Homann, H., Balloul, J.M., Villeval, D.,  
 771 Poitevin, Y., Kieny, M.P., *et al.* (2002). Tumor gene therapy by MVA-mediated expression of T-  
 772 cell-stimulating antibodies. *Cancer Gene Ther* 9, 470-477.  
 773 Pegram, H.J., Lee, J.C., Hayman, E.G., Imperato, G.H., Tedder, T.F., Sadelain, M., and  
 774 Brentjens, R.J. (2012). Tumor-targeted T cells modified to secrete IL-12 eradicate systemic  
 775 tumors without need for prior conditioning. *Blood* 119, 4133-4141.  
 776 Postow, M.A., Callahan, M.K., and Wolchok, J.D. (2015). Immune Checkpoint Blockade in  
 777 Cancer Therapy. *J Clin Oncol* 33, 1974-1982.  
 778 Rabinovich, G.A., Gabrilovich, D., and Sotomayor, E.M. (2007). Immunosuppressive strategies  
 779 that are mediated by tumor cells. *Annu Rev Immunol* 25, 267-296.  
 780 Rogakou, E.P., Pilch, D.R., Orr, A.H., Ivanova, V.S., and Bonner, W.M. (1998). DNA double-  
 781 stranded breaks induce histone H2AX phosphorylation on serine 139. *Journal of Biological*  
 782 *Chemistry* 273, 5858-5868.  
 783 Roybal, K.T., Rupp, L.J., Morsut, L., Walker, W.J., McNally, K.A., Park, J.S., and Lim, W.A.  
 784 (2016). Precision Tumor Recognition by T Cells With Combinatorial Antigen-Sensing Circuits.  
 785 *Cell* 164, 770-779.

786 Sadelain, M., Brentjens, R., and Riviere, I. (2013). The basic principles of chimeric antigen  
 787 receptor design. *Cancer Discov* 3, 388-398.  
 788 Sale, S., and Orsulic, S. (2006). Models of ovarian cancer metastasis: Murine models. *Drug*  
 789 *Discov Today Dis Models* 3, 149-154.  
 790 Satta, A., Mezzanzanica, D., Turatti, F., Canevari, S., and Figini, M. (2013). Redirection of T-  
 791 cell effector functions for cancer therapy: bispecific antibodies and chimeric antigen receptors.  
 792 *Future Oncol* 9, 527-539.  
 793 Schroeder, M.A., and DiPersio, J.F. (2011). Mouse models of graft-versus-host disease:  
 794 advances and limitations. *Dis Model Mech* 4, 318-333.  
 795 Schukur, L., and Fussenegger, M. (2016). Engineering of synthetic gene circuits for (re-  
 796 )balancing physiological processes in chronic diseases. *Wiley Interdiscip Rev Syst Biol Med* 8,  
 797 402-422.  
 798 Schukur, L., Geering, B., Charpin-El Hamri, G., and Fussenegger, M. (2015). Implantable  
 799 synthetic cytokine converter cells with AND-gate logic treat experimental psoriasis. *Sci Transl*  
 800 *Med* 7, 318ra201.  
 801 Schumacher, T.N., and Schreiber, R.D. (2015). Neoantigens in cancer immunotherapy. *Science*  
 802 348, 69-74.  
 803 Selvakumaran, M., Bao, R., Crijns, A.P., Connolly, D.C., Weinstein, J.K., and Hamilton, T.C.  
 804 (2001). Ovarian epithelial cell lineage-specific gene expression using the promoter of a  
 805 retrovirus-like element. *Cancer Res* 61, 1291-1295.  
 806 Shukla, S., and Steinmetz, N.F. (2016). Emerging nanotechnologies for cancer immunotherapy.  
 807 *Exp Biol Med (Maywood)* 241, 1116-1126.  
 808 Suzuki, H.I., Katsura, A., Yasuda, T., Ueno, T., Mano, H., Sugimoto, K., and Miyazono, K.  
 809 (2015). Small-RNA asymmetry is directly driven by mammalian Argonautes. *Nature Structural*  
 810 *& Molecular Biology* 22, 512-521.  
 811 Szymczak, A.L., Workman, C.J., Wang, Y., Vignali, K.M., Dilioglou, S., Vanin, E.F., and  
 812 Vignali, D.A. (2004). Correction of multi-gene deficiency in vivo using a single 'self-cleaving'  
 813 2A peptide-based retroviral vector. *Nat Biotechnol* 22, 589-594.  
 814 Tugues, S., Burkhard, S.H., Ohs, I., Vrohling, M., Nussbaum, K., Vom Berg, J., Kulig, P., and  
 815 Becher, B. (2015). New insights into IL-12-mediated tumor suppression. *Cell Death Differ* 22,  
 816 237-246.  
 817 Turley, S.J., Cremasco, V., and Astarita, J.L. (2015). Immunological hallmarks of stromal cells  
 818 in the tumour microenvironment. *Nature Reviews Immunology* 15, 669-682.  
 819 van der Burg, S.H., Arens, R., Ossendorp, F., van Hall, T., and Melief, C.J. (2016). Vaccines for  
 820 established cancer: overcoming the challenges posed by immune evasion. *Nat Rev Cancer*.  
 821 von Nickisch-Rosenegk, M., Teschke, T., and Bier, F.F. (2012). Construction of an artificial cell  
 822 membrane anchor using DARC as a fitting for artificial extracellular functionalities of eukaryotic  
 823 cells. *J Nanobiotechnology* 10, 1.  
 824 Wei, P., Wong, W.W., Park, J.S., Corcoran, E.E., Peisajovich, S.G., Onuffer, J.J., Weiss, A., and  
 825 Lim, W.A. (2012). Bacterial virulence proteins as tools to rewire kinase pathways in yeast and  
 826 immune cells. *Nature* 488, 384-+.  
 827 Xie, M., Ye, H., Wang, H., Charpin-El Hamri, G., Lormeau, C., Saxena, P., Stelling, J., and  
 828 Fussenegger, M. (2016). beta-cell-mimetic designer cells provide closed-loop glycemic control.  
 829 *Science* 354, 1296-1301.  
 830 Xie, Z., Wroblewska, L., Prochazka, L., Weiss, R., and Benenson, Y. (2011). Multi-Input RNAi-  
 831 Based Logic Circuit for Identification of Specific Cancer Cells. *Science* 333, 1307-1311.

Yang, Z.M., Li, E.M., Lai, B.C., Wang, Y.L., and Si, L.S. (2007). Anti-CD3 scFv-B7.1 fusion protein expressed on the surface of HeLa cells provokes potent T-lymphocyte activation and cytotoxicity. *Biochem Cell Biol* 85, 196-202.

Yun, H.J., Cho, Y.H., Moon, Y., Park, Y.W., Yoon, H.K., Kim, Y.J., Cho, S.H., Lee, Y.I., Kang, B.S., Kim, W.J., *et al.* (2008). Transcriptional targeting of gene expression in breast cancer by the promoters of protein regulator of cytokinesis 1 and ribonuclease reductase 2. *Exp Mol Med* 40, 345-353.

Zaharoff, D.A., Hance, K.W., Rogers, C.J., Schlom, J., and Greiner, J.W. (2010). Intratumoral immunotherapy of established solid tumors with chitosan/IL-12. *J Immunother* 33, 697-705.

Zhang, L., Morgan, R.A., Beane, J.D., Zheng, Z., Dudley, M.E., Kassim, S.H., Nahvi, A.V., Ngo, L.T., Sherry, R.M., Phan, G.Q., *et al.* (2015). Tumor-infiltrating lymphocytes genetically engineered with an inducible gene encoding interleukin-12 for the immunotherapy of metastatic melanoma. *Clin Cancer Res* 21, 2278-2288.

Zhang, W., Fulci, G., Wakimoto, H., Cheema, T.A., Buhrman, J.S., Jeyaretna, D.S., Stemmer Rachamimov, A.O., Rabkin, S.D., and Martuza, R.L. (2013). Combination of oncolytic herpes simplex viruses armed with angiostatin and IL-12 enhances antitumor efficacy in human glioblastoma models. *Neoplasia* 15, 591-599.

Zhou, D., Cutlar, L., Gao, Y., Wang, W., O'Keeffe-Ahern, J., McMahon, S., Duarte, B., Larcher, F., Rodriguez, B.J., and Greiser, U. (2016). The transition from linear to highly branched poly(beta-amino ester)s: Branching matters for gene delivery. *Sci Adv* 2, e1600102.

**Figure 1**

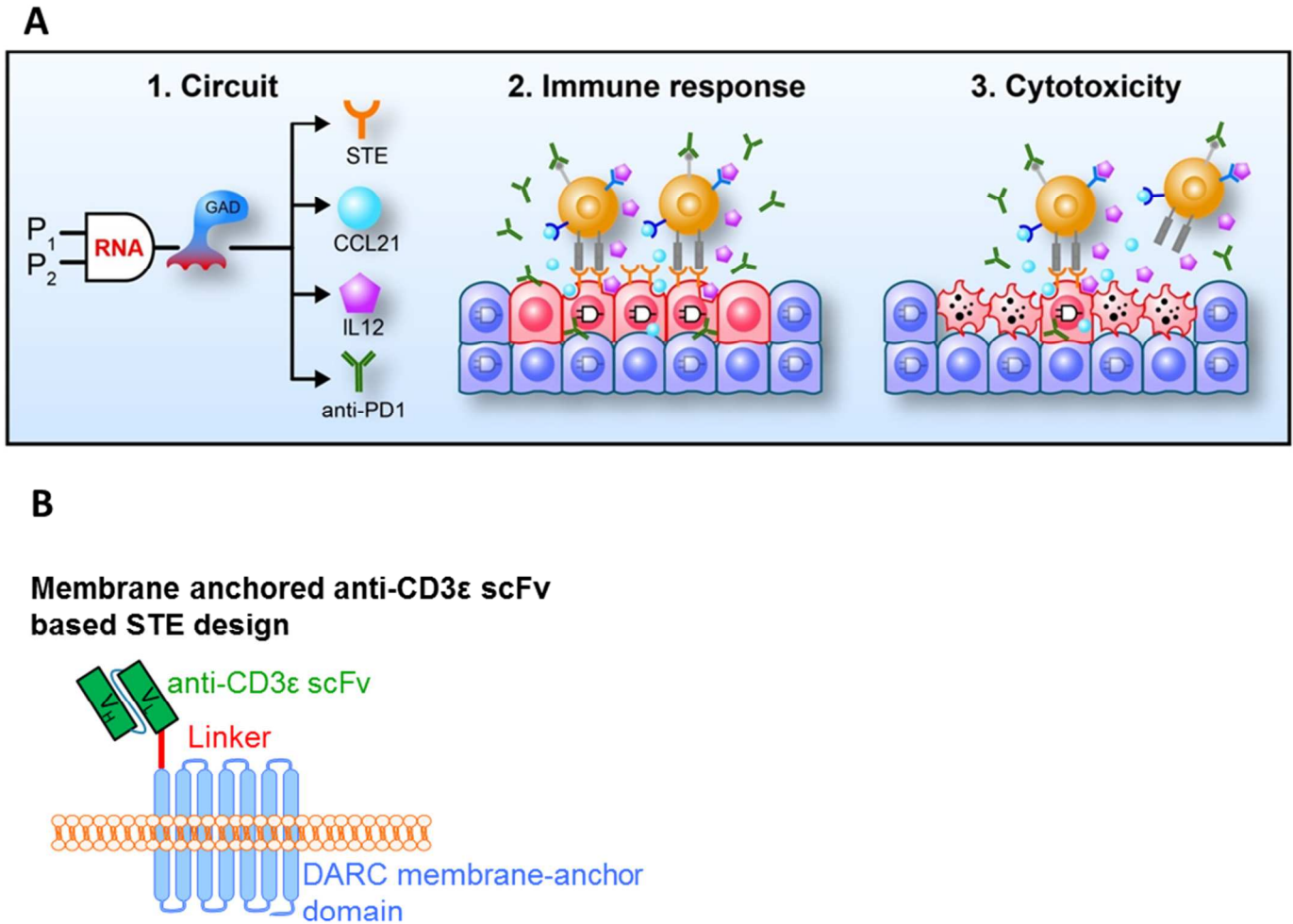


**Figure 1.** Immunomodulatory synthetic gene circuits are programmed to be selectively activated in cancer cells.

**(A) Panel 1:** Immunomodulatory synthetic gene circuits are designed to integrate the activity of two tumor-specific synthetic promoters ( $P_1$  and  $P_2$ ) with an RNA-based AND gate mechanism and generate combinatorial immunomodulator outputs only when input promoters are mutually active. When activated, the AND gate expresses a synthetic transcription factor (GAD: a fusion protein consisting of the GAL4 DNA binding domain and VP16 transcription activating domain), which drives the co-expression of combinatorial immunomodulators, including Surface T-cell Engagers (STEs, which are anti-CD3 $\epsilon$  scFvs displayed on the cell surface) and secreted CCL21, IL12, and an anti-PD1 antibody. **Panel 2:** The circuits are triggered to express immunomodulators in cancer cells (red), but not normal cells (blue) (Black-line circuit diagrams indicate circuits are active and Grey-line circuit diagrams indicate circuits are inactive). **Panel 3:** Cancer-specific expression of combinatorial immunomodulators triggers effective T-cell mediated killing of the cancer cells.

**(B)** Schematic drawing of STE displayed on cell surfaces. DARC refers to the silent Duffy antigen/receptor for chemokines.



**Figure 2**

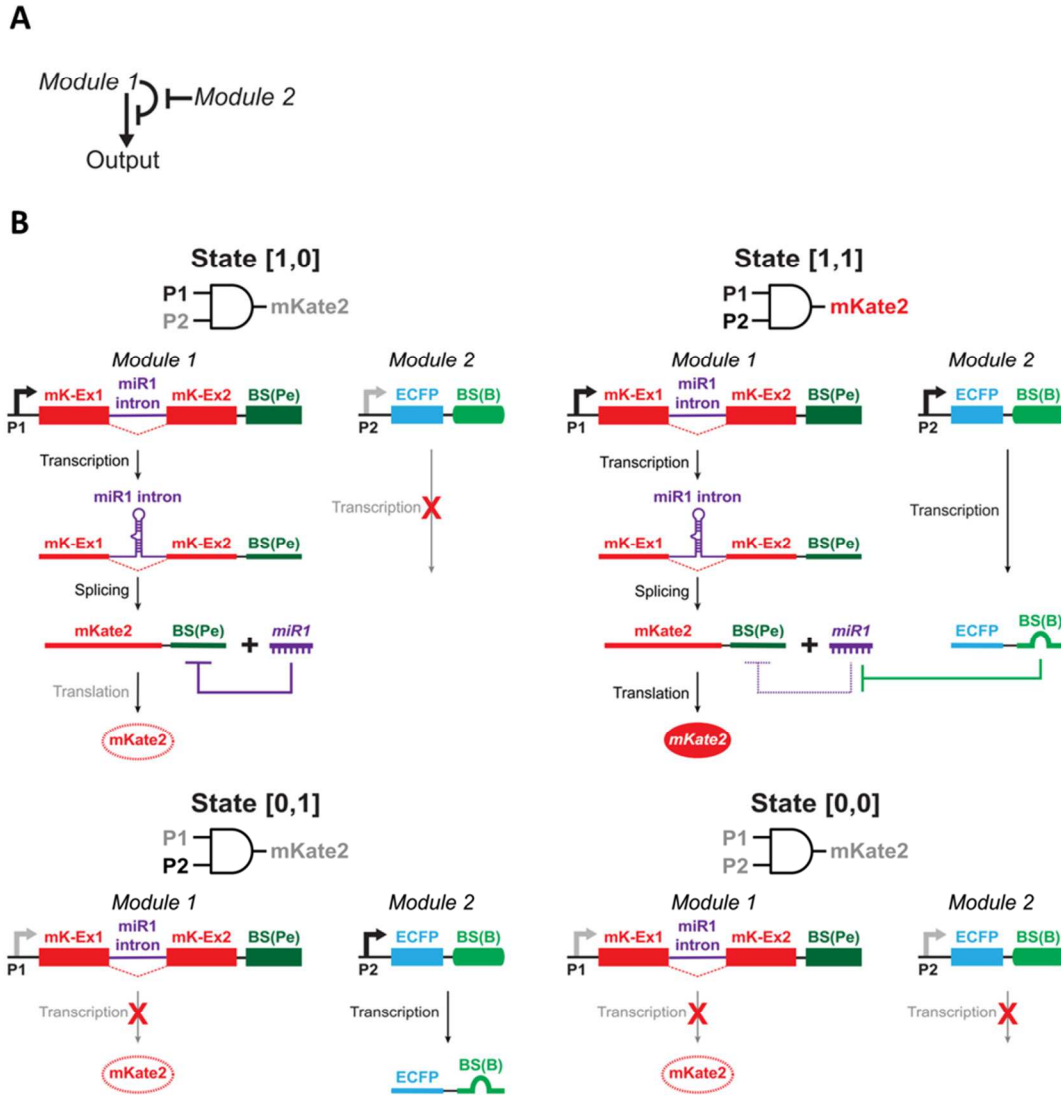


**Figure 2.** The basic RNA-only single-output AND gate design.

(A) *Module 1* of the AND gate is designed as an auto-inhibitory loop such that it represses its own output. *Module 2* is designed to inhibit the auto-inhibition of *Module 1*. *Module 1* and *Module 2* are regulated by cancer-specific promoters P1 and P2, respectively. The output from *Module 1* is expressed at a high level only when both P1 and P2 are active, which enhances the tumor specificity of the circuit.

(B) All 4 possible input states and their respective output states are shown for the RNA-only single-output AND gate. Input states are defined within the square brackets by whether *Module 1* and *Module 2* are active, where 0 means inactive and 1 means active. In State [1,0], P1 is active and the mKate2 transcript is expressed (mK-Ex1 and mK-Ex2 denote mKate2 exon1 and mKate2 exon2, respectively). However, this transcript encodes an intronic synthetic miRNA (miR1) within the mKate2 gene that inhibits the mKate2 transcript by targeting perfect match miR1 binding sites (BS(Pe)) in the 3' untranslated region. Thus, the mKate2 levels are minimal. In State [0,1], P1 is inactive so the output protein mKate2 is not expressed. In State [0,0], neither P1 nor P2 are active and thus the output protein mKate2 is not expressed. In State [1,1], the P2 promoter expresses a sponge for miR1 that is based on bulged miR1 binding sites (BS(B)). This enables sequestration of miR1 away from inhibiting the mKate2 transcript expressed by P1, thus allowing for mKate2 expression.

**Figure 3**

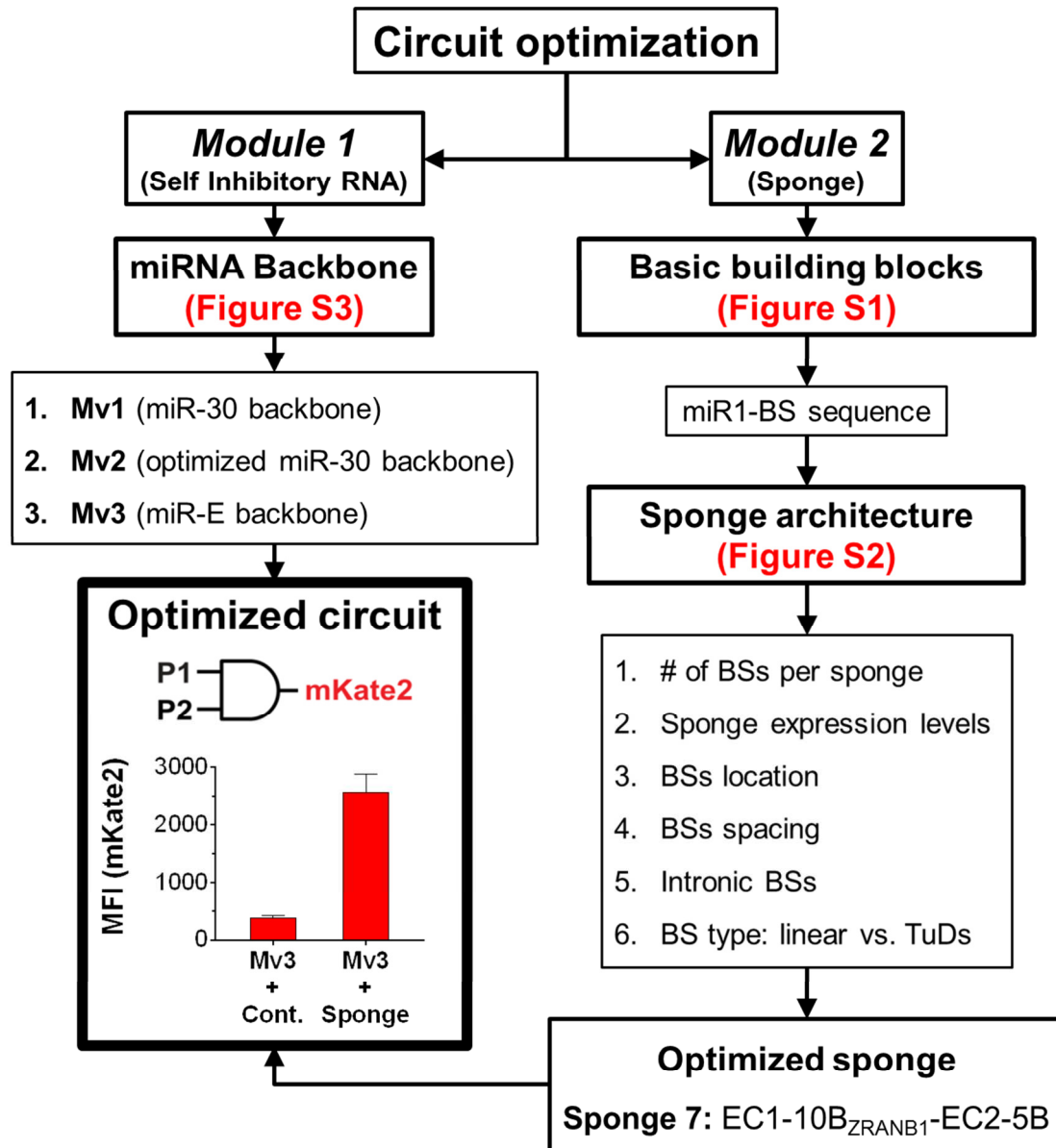


**Figure 3.** Flowchart of circuit optimization strategies for the RNA-based AND gate.

Specific details are described in Supplementary Information and Figure S1-3. Multiple versions of the miR1 production backbone in *Module 1* as well as the miR1 binding-site sequences (BSs) and sponge architecture in *Module 2* were systematically tested. The optimized circuit utilized the miR-E backbone (Mv3, Table S2) in *Module 1* to generate miR1 and a sponge architecture in *Module 2* that encoded 10 optimized bulged miR1 binding sites within an ECFP gene (EC1-10B<sub>ZRANB1</sub>-EC2) and 5 additional bulged miR1 binding sites (5B) in the downstream 3'UTR (Figure S2A). The mKate2 output levels for the optimized circuit with a control sponge with no miR1 binding sites ('Mv3 + Cont.', representing the [1,0] state in Figure 2C), and the optimized circuit with the optimized sponge ('Mv3 + Sponge', corresponding to Sponge 7 from Figure S2A, representing the [1,1] state in Figure 2C) are shown. *Module 1* was expressed by SSX1p and *Module 2* was expressed by H2A1p. Error bars represent S.E.M., N = 3 biological replicates. MFI = Mean Fluorescence Intensity. BS = binding sites. TuD = tough-decoy architecture.

See also Figure S1-3.

**Figure 4**

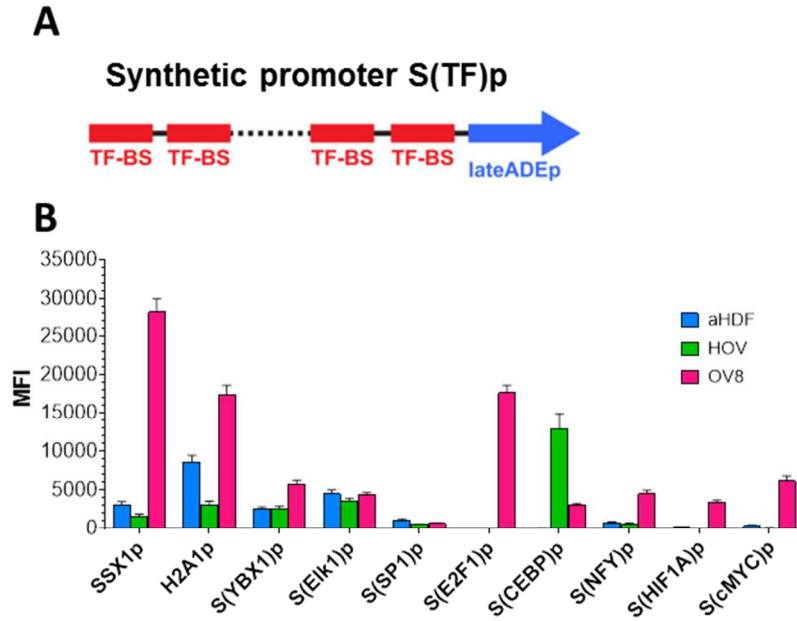
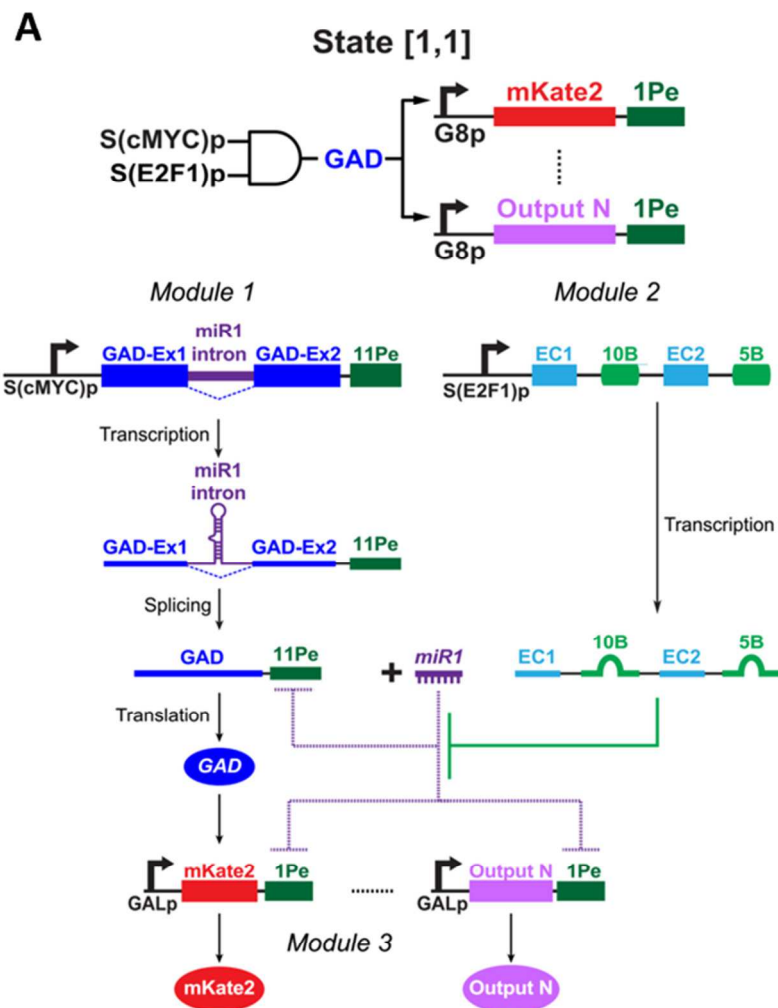
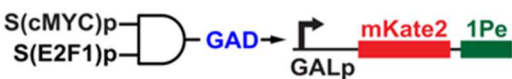


**Figure 4.** Synthetic tumor-specific promoters exhibited high tumor specificity.

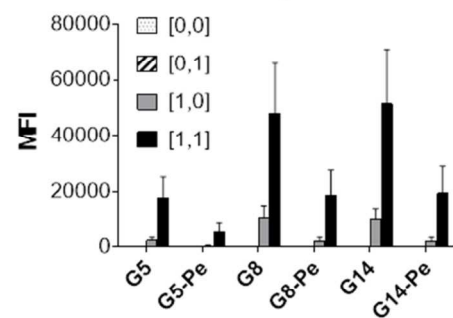
(A) Design of synthetic tumor-specific promoters, S(TF)p. Multiple binding sites for a transcription factor that is over-expressed in cancer (TF-BS) were cloned in tandem upstream of a minimal lateADEp promoter (late adenovirus promoter).

(B) Synthetic tumor-specific promoters regulating mKate2 exhibited enhanced tumor specificity. Representative native tumor-specific promoters, SSX1p and H2A1p, are shown for comparison. Parentheses indicate the transcription factor binding sites used to construct each synthetic tumor-specific promoter. aHDF (adult human dermal fibroblast) and HOV (human ovarian epithelium) are normal primary cells. OV8 (OVCAR8) is a human ovarian cancer cell line.

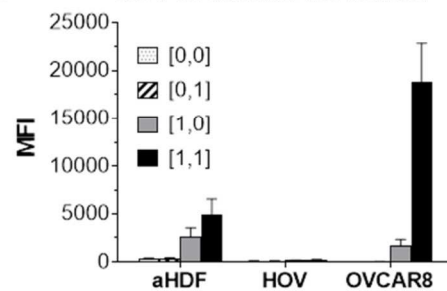
Figure 5



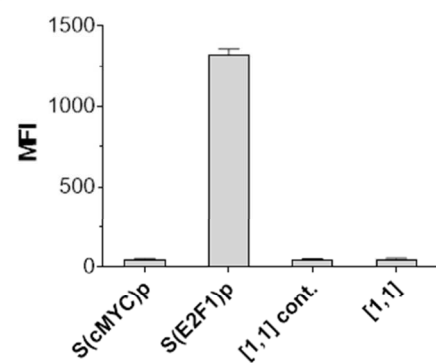
**B** Circuit design: OVCAR8



**C** G8-Pe: normal vs. cancer



**D** G8-Pe: T-cells



**E** G8-Pe: normal vs. cancer

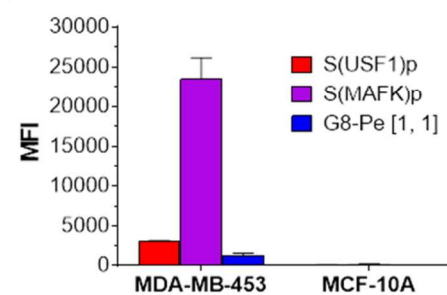


**Figure 5.** Multi-output AND gate architecture and performance.

(A) The incorporation of a synthetic transcription factor (GAD) as the output of *Module 1* means that it is only expressed at high levels when both P1 and P2 are high (state [1,1]). GAD enables facile tuning of downstream gene expression (mKate2 ... Output N).

(B) mKate2 expression can be modulated by modifying the number of GAD binding sites in the synthetic GALp promoter expressing mKate2 (G5, G8, G14 for 5, 8, 14 GAD binding sites in GALp) and the presence of miRNA binding sites at the mKate2 3'UTR (G5-Pe, G8-Pe, G14-Pe indicate transcripts with a perfect match miR1 binding site). Note the circuit diagram depicts the version with a perfect miR1 binding site in the mKate2 transcript. State [0,0] indicates cells containing the negative control modules, *Module 1con* and *Module 2con* (see text for details). State [0,1] indicates cells containing *Module 1con* and *Module 2*. State [1,0] indicates cells containing *Module 1* and *Module 2con*. State [1,1] indicates cells containing *Module 1* and *Module 2*. All cell states tested also contained their respective *Module 3*.

(C) The G8-Pe AND gate architecture triggered high mKate2 expression in human ovarian cancer cells (OV8) but not in normal cells in state [1,1].

(D) Our circuit design prevents potential off-target effects in primary human T cells. The S(E2F1)p promoter was active in T cells but S(cMYC)p was inactive in T cells. The G8-Pe circuit triggered minimal mKate2 output in T cells, thus minimizing the potential off-target effects that would have been observed if the S(E2F1)p was used to directly drive mKate2 expression.

(E) Our circuit design can be readily adapted to distinguish a different tumor type from its normal counterparts. By using two different promoters, the G8-Pe circuit triggered a strong output in the breast cancer cell line MDA-MB-453 but minimal output in the non-tumorigenic breast epithelial cell line MCF-10A.

Error bars represent S.E.M., N = 3 biological replicates for all experiments except N = 6 biological replicates for OVCAR8 group in Figure 5C.

See also Figure S4A.

Figure 6

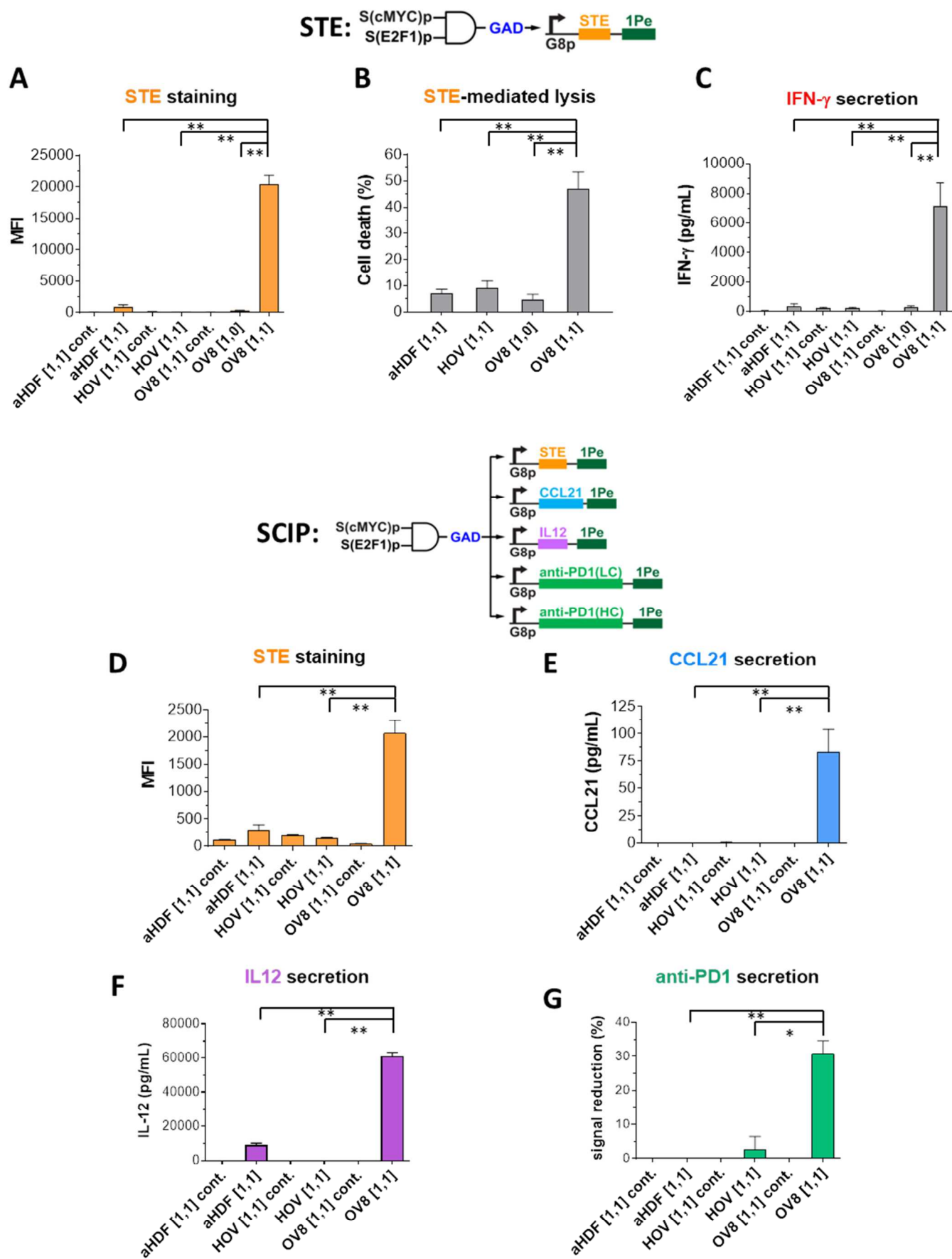


**Figure 6.** Synthetic circuits triggered human ovarian cancer-specific expression of STE, T-cell mediated lysis and IFN- $\gamma$  secretion on tumor cells. aHDF (adult human dermal fibroblast) and HOV (human ovarian epithelium) are normal primary cells.

**(A)-(C)** The circuit in Figure 5A was engineered to display STE on cell surfaces as the output. STE was encoded in *Module 3*. State '[1,1] cont.' indicates cells containing *Module 1* and *Module 2* and a negative control *Module 3con* that expresses the non-specific transcription factor rtTA3 as the output. State [1,1] indicates cells containing *Module 1*, *Module 2*, and *Module 3*. State [1,0] indicates cells containing *Module 1*, a negative control *Module 2con* in which S(E2F1)p expresses ECFP without miR1-BS(B), and *Module 3*. Circuit-transduced tumor cells but not normal cells expressed high levels of STE in state [1,1], which triggered robust T-cell killing and IFN- $\gamma$  secretion. Student's t-test was performed to compare the [1,1] states between normal cells and OV8 cells, and the [1,1] state versus the [1,0] state in OV8 cells.

**(D)-(G)** Synthetic circuits triggered human ovarian cancer-specific expression of combinatorial immunomodulators. The circuit in Figure 5A was extended to express multiple immunomodulatory outputs (surface-displayed STE and secreted CCL21, IL12, and anti-PD1 Ab) specifically in OV8 cells but not normal primary cells. State '[1,1] cont.' indicates cells containing *Module 1* and *Module 2* and a negative control *Module 3con* that expresses the non-specific transcription factor rtTA3 as the output. State [1,1] indicates cells containing *Module 1*, *Module 2*, and *Module 3*. Each immunomodulatory gene was expressed from its own G8p promoter encoded on a lentivirus, except for the anti-PD1 Ab, which was split into two lentiviruses encoding light chain (LC) and heavy chain (HC) respectively. Cell lines were co-infected with these lentiviral constructs. Student's t-test was performed to compare output levels in the [1,1] states between normal cells and OV8 cells.

Error bars represent S.E.M., N = 3 biological replicates (\*  $p < 0.05$ ; \*\*  $p < 0.005$ ).

See also Figure S4.

Figure 7

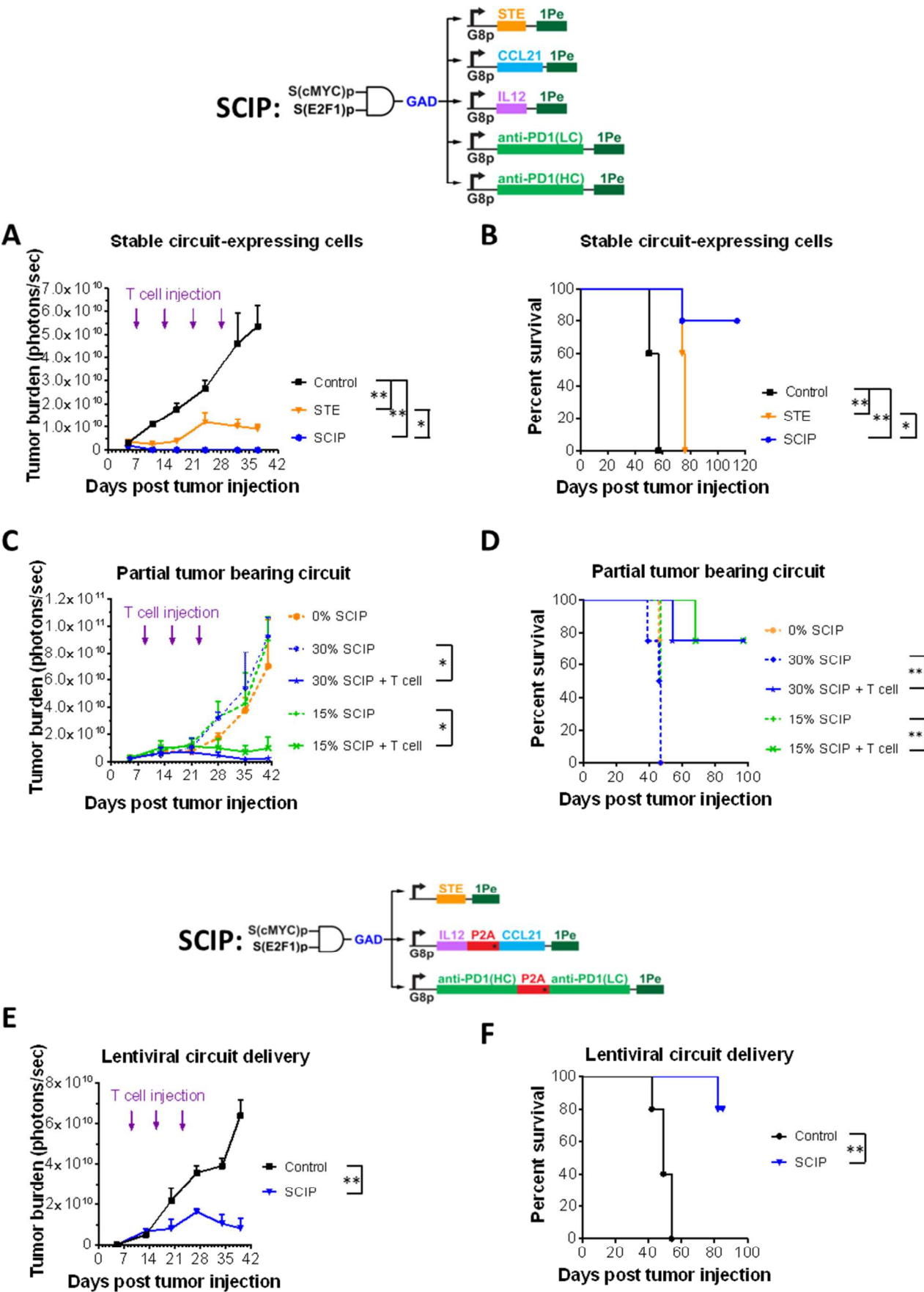




**Figure 7.** Combination immunotherapies triggered by cancer-specific circuits significantly reduced tumor burden and increased survival in an intraperitoneally disseminated human ovarian cancer model in mice.

**(A)** OV8 cells were transduced with constructs encoding a control output rtTA3 (Control), STE-only (STE), or combination immunomodulators (SCIP). All groups were implanted into NSG mice and injected periodically with human T cells. Student's t-test was performed to compare tumor burden between groups at day 37. Error bars represent S.E.M., N = 5 biological replicates.

**(B)** Kaplan-Meier survival curves of various groups (N = 5 biological replicates). A log-rank (Mantel-Cox) test was performed to compare survival between groups.

**(C)** Robust therapeutic efficacy was achieved even when only 15% or 30% of tumor cells were transduced with the SCIP circuit (the remaining implanted cancer cells were wild-type OV8). Therapeutic efficacy was dependent on the presence of T cells. Student's t-test was performed to compare tumor burden between groups at day 41. Error bars represent S.E.M., N = 4 biological replicates.

**(D)** Kaplan-Meier survival curves of various groups with different percentages of the overall tumor cells transduced with the SCIP circuit (N = 4 biological replicates). A log-rank (Mantel-Cox) test was performed to compare survival between groups.

**(E)** Lentiviral delivery of the SCIP-expressing circuit significantly reduced ovarian cancer burden. NSG mice were injected with OVCAR8 cells into the peritoneal space at day 0. Lentiviruses encoding circuit *Module 1* and *Module 2* and a control output rtTA3 (Control), or combination immunomodulators (SCIP) were then injected *i.p.* on day 7. These mice were also injected *i.p.* periodically (day 9, 16, and 23) with human T cells. Student's t-test was performed to compare tumor burden between groups at day 39. Error bars represent S.E.M., N = 5 biological replicates.

**(F)** Kaplan-Meier survival curves of various groups (N = 5 biological replicates). A log-rank (Mantel-Cox) test was performed to compare survival between groups.

(\*  $p < 0.05$ ; \*\*  $p < 0.005$ ).

See also Figure S5-7.

Figure S1

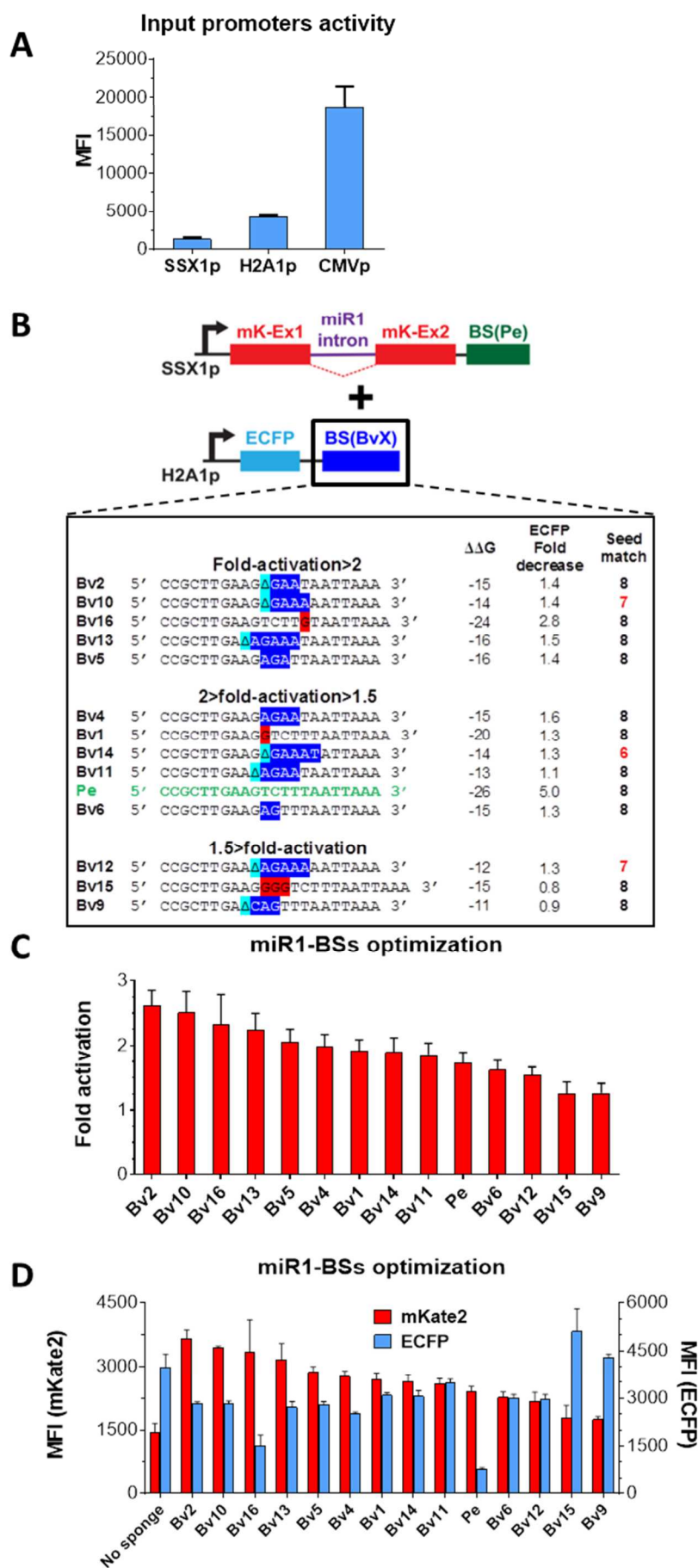


**Figure S1.** Optimization of the miRNA binding-site sequences in the sponge in *Module 2*, related to Figure 3.

**(A)** The activity of the promoters SSX1p, H2A1p, and CMVp in HEK-293T cells.

**(B)-(C)** Various miRNA binding sequences (miR1-BSs) used in the sponge affect sponging activity, assayed by mKate2 fold-activation by each sponge (state [1,1] versus state [1,0] in Figure 2B). Nucleotides highlighted in dark blue are mismatched nucleotides. Nucleotides highlighted in red are insertions. Light blue capital-delta ( $\Delta$ ) indicates deleted nucleotides. SSX1p was used to drive *Module 1* expression and H2A1p was used to drive *Module 2* expression. *Module 1* encoded a transcript with miR1 as an intron within the mKate2 gene, where miR1 targeted 3 perfect match miR1-BS encoded downstream of mKate2. *Module 2* encoded the miR1 sponges, described above, downstream of an ECFP gene.

**(D)** MFI of mKate2 and ECFP in binding site optimization experiments. Error bars represent S.E.M., N = 3 biological replicates. MFI = Mean Fluorescence Intensity.

Figure S2

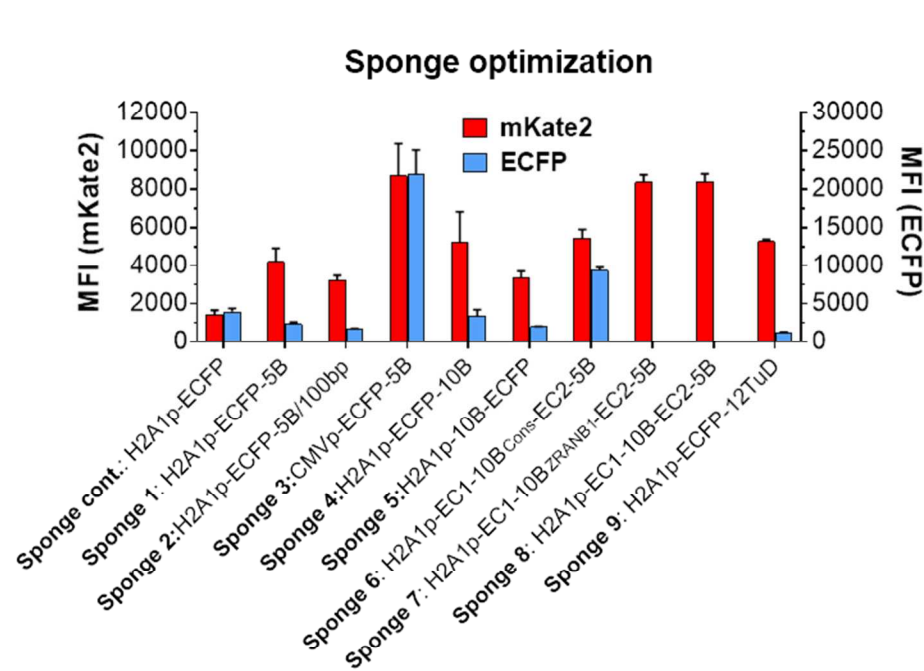
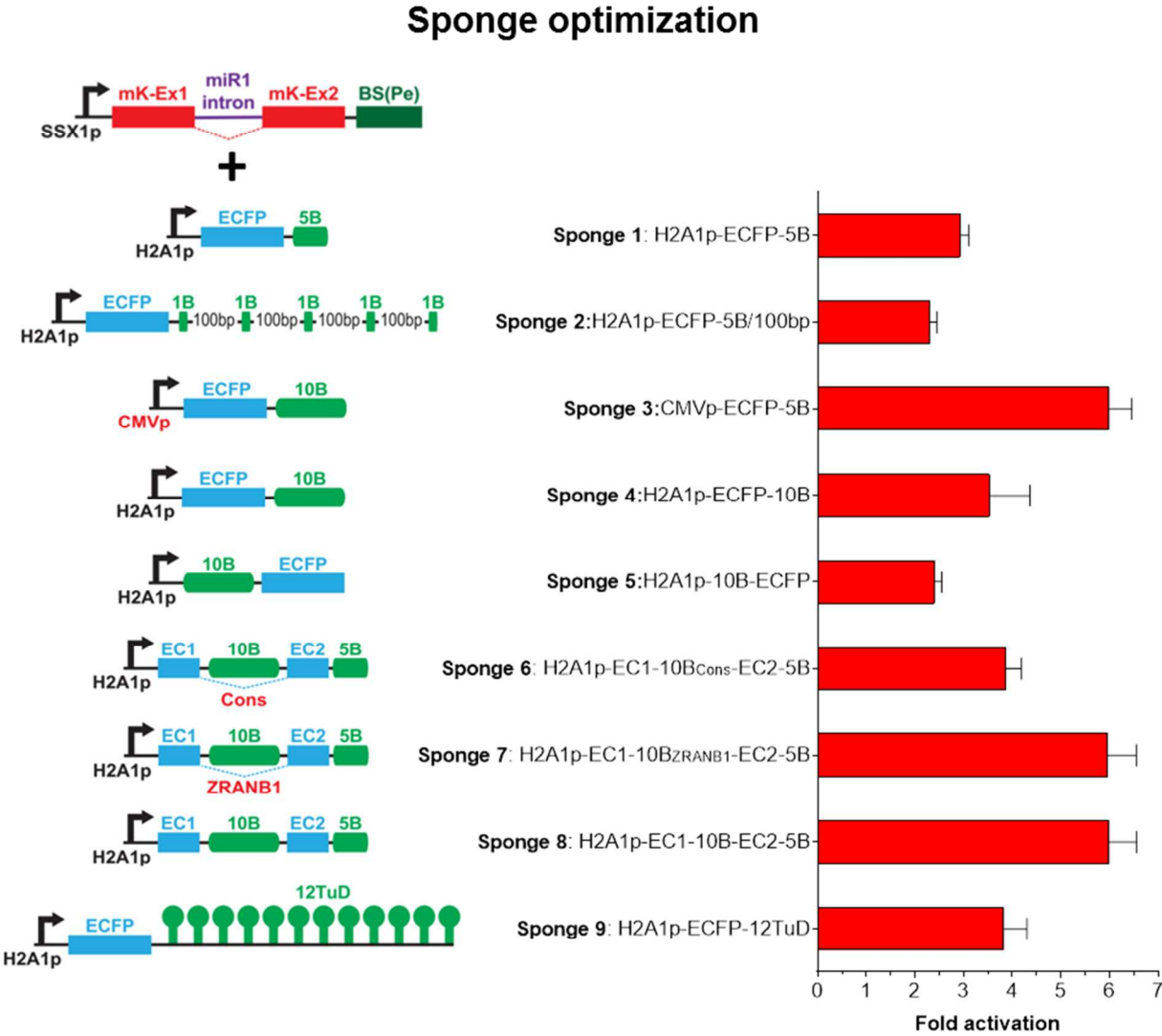


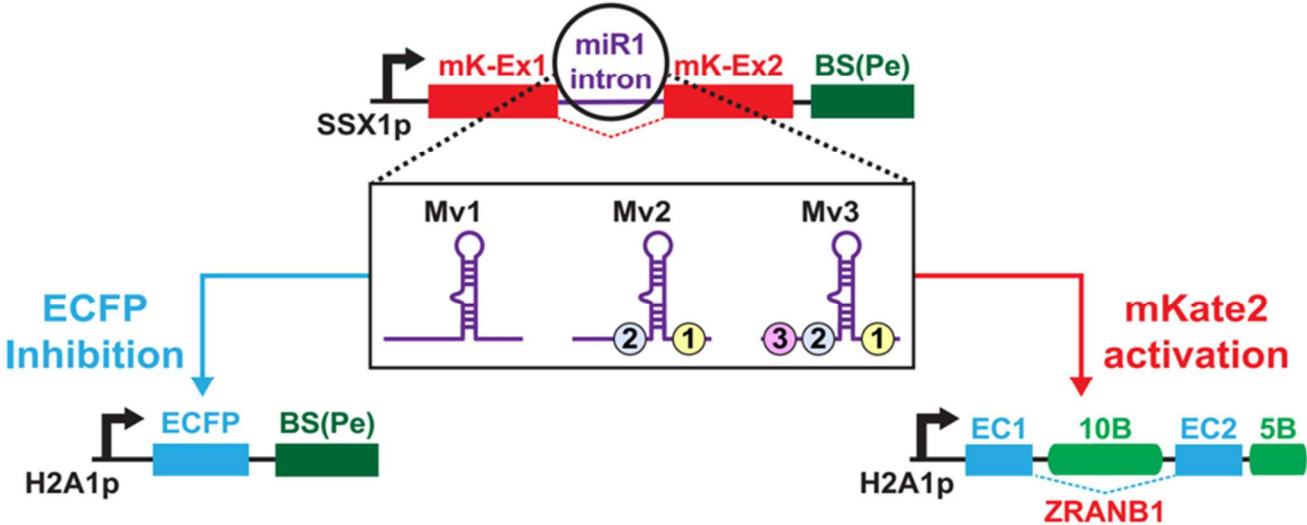
**Figure S2.** Optimization of the sponge architecture in *Module 2*, related to Figure 3.

(A) The number of miRNA binding sites, the sponge expression level, and the architecture of the sponge affect sponging activity. Fold activation was assayed by mKate2 fold-activation by each sponge (state [1,1] versus state [1,0] in Figure 2B). SSX1p was used to drive *Module 1* expression and H2A1p or CMVp was used to drive *Module 2* expression, as indicated. *Module 1* encoded a transcript with miR1 as an intron within the mKate2 gene, where miR1 targeted 3 perfect match miR1-BS encoded downstream of mKate2. *Module 2* encoded the miR1 sponges. 5B and 10B refers to 5 or 10 bulged miR1 binding sites in the sponge based on the Bv2 design from Figure S1B. EC1 and EC2 correspond to exon 1 and exon 2 of ECFP and constructs in which 10B was encoded within the ECFP transcript with different architectures (Cons and ZRANB1). 12TuD (Tough Decoy) architecture refers to 24 miR1-BSs encoded within 12 loop of an RNA hairpin (2 miR1-BSs per hairpin loop). 5B/100 bp refers to 5 bulged miR1-BSs separated by 100bp linkers rather than 5bp in all other sponges. Error bars represent S.E.M., N = 3 biological replicates.

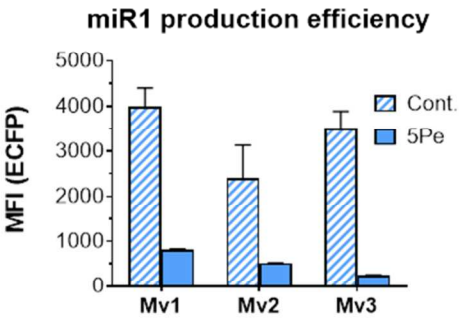
(B) MFI of mKate2 and ECFP in sponge architecture optimization experiments.

Figure S3

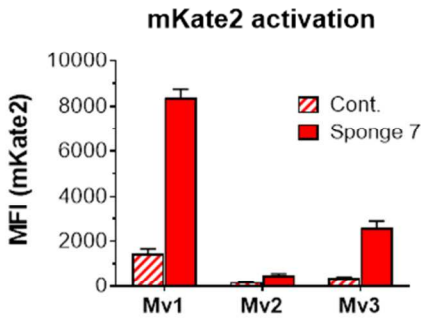
A



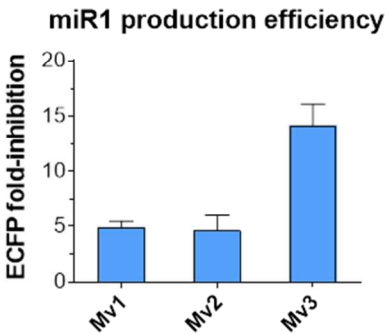
B



D



C



E

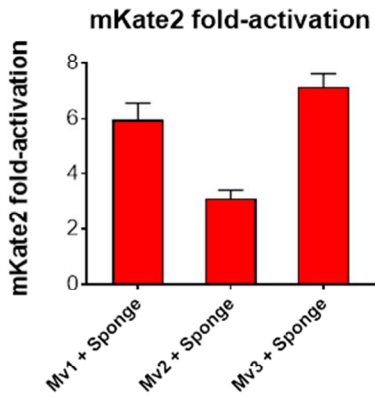


**Figure S3.** pri-miRNA backbones used to produce miR1 from *Module 1* affect circuit performance, related to Figure 3.

**(A)** *Module 1* variants Mv1-Mv3 expressed a transcript in which the different miR1 pri-miRNA architectures shown were encoded as an intron within the mKate2 gene, where miR1 then targeted 3 perfect match miR1-BS encoded downstream of mKate2. The colored circles denote the location of the insertion sequences for creating Mv2 and Mv3 (See Table S2 for detailed sequences and functional pri-miRNA modifications).

**(B-E)** Different pri-miRNA backbones modulate the production of miRNA and the ON:OFF ratio of the circuit.

**(B-C)** We tested the three different *Module 1* variants together with *Module 2* variations composed of a control sponge with no miR1 binding sites ('Cont.') and a sponge with 5 perfect match miR1 binding sites downstream to an ECFP gene ('5Pe'). *Module 1* was expressed by SSX1p and *Module 2* was expressed by H2A1p. Mv1-Mv3 exhibited different miR1 production efficiencies, as measured by ECFP signal reduction with the 5Pe *Module 2* compared to ECFP signal in the control *Module 2*; Mv3 had the most efficient miR1 production.

**(D-E)** mKate2 expression levels with control sponge or the optimized sponge ('Sponge 7', *Sponge 7* from Figure S2A). Mv3 exhibited a low mKate2 level in the OFF state and the highest fold-activation by the sponge in the ON state.

Error bars represent S.E.M., N = 3 biological replicates.

**Figure S4**

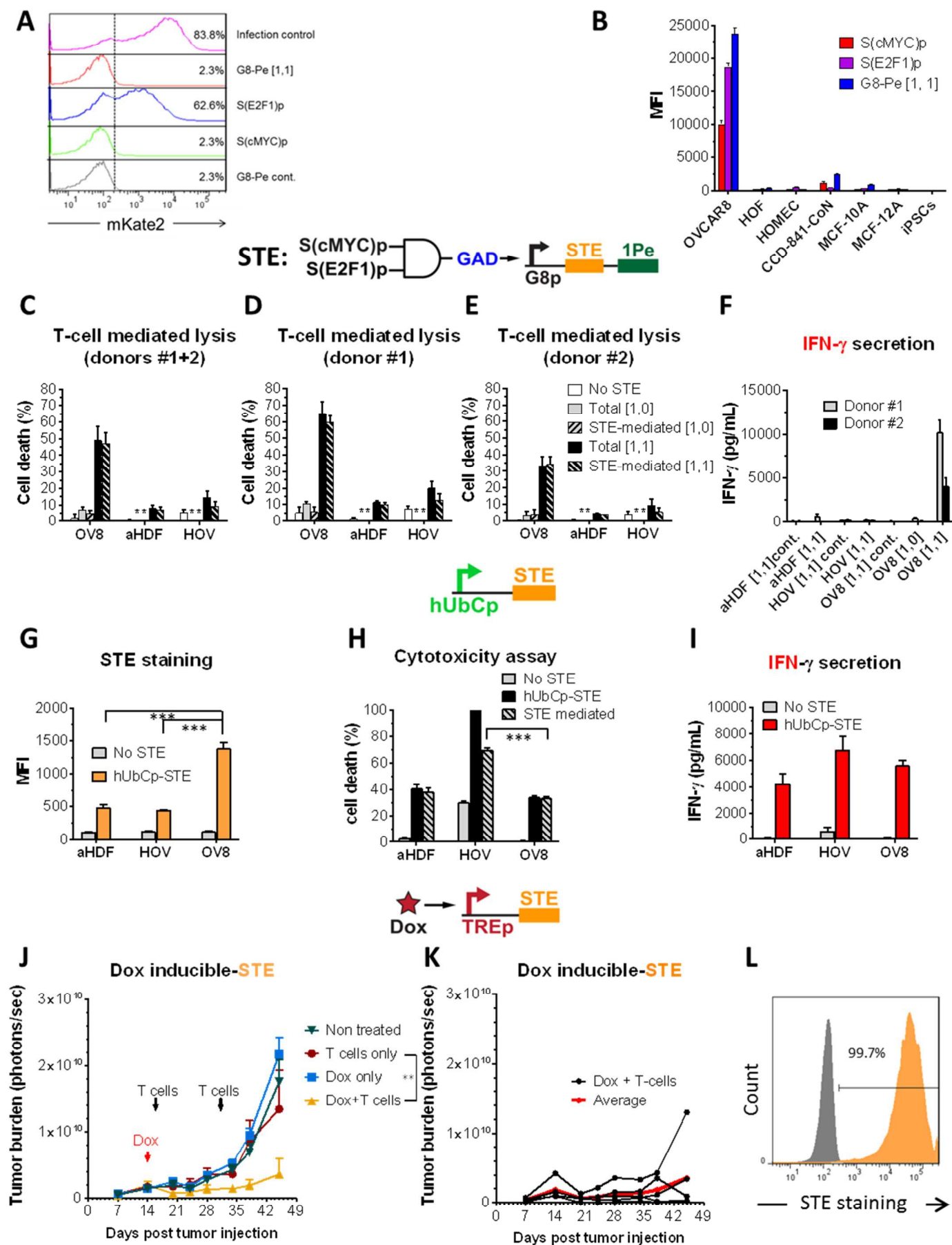




**Figure S4.** Multi-output circuit specifically triggered T cells to kill ovarian tumor cells and secrete IFN- $\gamma$ , related to Figure 5-6.

**(A)** FACS histograms showing the activity of single promoters and the G8-Pe circuit when transduced into T cells via lentivirus. The percentages on the histograms denote the percent of cells with higher mKate2 expression level than the value of the dotted line. A constitutive human Ubiquitin C promoter expressing mKate2 was used for the “infection control” group.

**(B)** S(cMYC)p, S(E2F1)p, and the G8-Pe circuit exhibit high activity in OV8 cells but not in various non-tumorigenic cell lines. OV8 is an ovarian cancer cell line. HOF (human ovarian fibroblasts), HOMEc (human ovarian microvasculature epithelial cells), CCD-841-CoN (non-tumorigenic colonic epithelial cells), and MCF-10A and MCF-12A (non-tumorigenic mammary epithelial cells), are non-tumorigenic cell lines. iPSCs = inducible pluripotent stem cells.

**(C-E)** T-cell mediated killing of G8-Pe circuit-transduced tumor cells was significantly greater than of normal cells. The percentage of cell death mediated by T cells from donor #1 (**D**), donor #2 (**E**) and the calculated mean (**C**) are shown. \* indicates condition not tested. Note that total cell death and STE-mediated cell death of the [1,0] state in aHDF and HOV cells were not measured because this state simulates a condition in which only one of the input promoters is active and is expected to result in lower killing than state [1,1], in which both input promoters are active. Total cell death and STE-mediated cell death correspond to uncorrected cell death and background-killing corrected cell death, respectively. See Methods for more details.

**(F)** G8-Pe circuit-transduced tumor cells trigger robust IFN- $\gamma$  secretion by T cells. Data shown represent IFN- $\gamma$  levels secreted by T cells from donor #1 and donor #2. Error bars represent S.E.M., N = 3 biological replicates.

**(G-I)** aHDF, HOV, and OV8 constitutively displaying STE can trigger robust STE-mediated killing and IFN- $\gamma$  secretion by T cells. A constitutive human Ubiquitin C promoter (hUbCp) was used to drive STE expression on aHDF, HOV, and OV8. All three cell lines displayed STE and triggered strong STE-mediated cell killing and IFN- $\gamma$  secretion by T cells. Error bars represent S.E.M., N = 3 biological replicates.

**(J)** Doxycycline (Dox)-inducible expression of STE triggered significant T-cell-mediated killing *in vivo*. Inducible display of STE with doxycycline (Dox) on the surface of OV8 cells triggered human T-cell-mediated killing *in vivo* in a mouse model of disseminated intraperitoneal ovarian cancer. Anti-tumor activity was abrogated when STEs were not displayed (T cells only) or T cells were not injected (Dox only). Student's t-test was used to compare tumor burdens between groups at day 45. Error bars represent S.E.M., N = 5 biological replicates

**(K)** Tumor burden of individual mice (black) and mean (red) of the Dox + T cell group in Figure S4J.

**(L)** OV8 cells engineered with a Dox-inducible STE construct expressed high levels of STE on their cell surfaces after induction. Histograms of STE staining on OV8 cells are shown. The gray and orange histograms represent the staining of uninduced OV8 and Dox-induced OV8 cells, respectively. Data shown are representative histograms, which were repeated in 3 independent experiments.

(\*  $p < 0.05$ ; \*\*  $p < 0.005$ ; \*\*\*  $p < 0.001$ ).

**Figure S5**

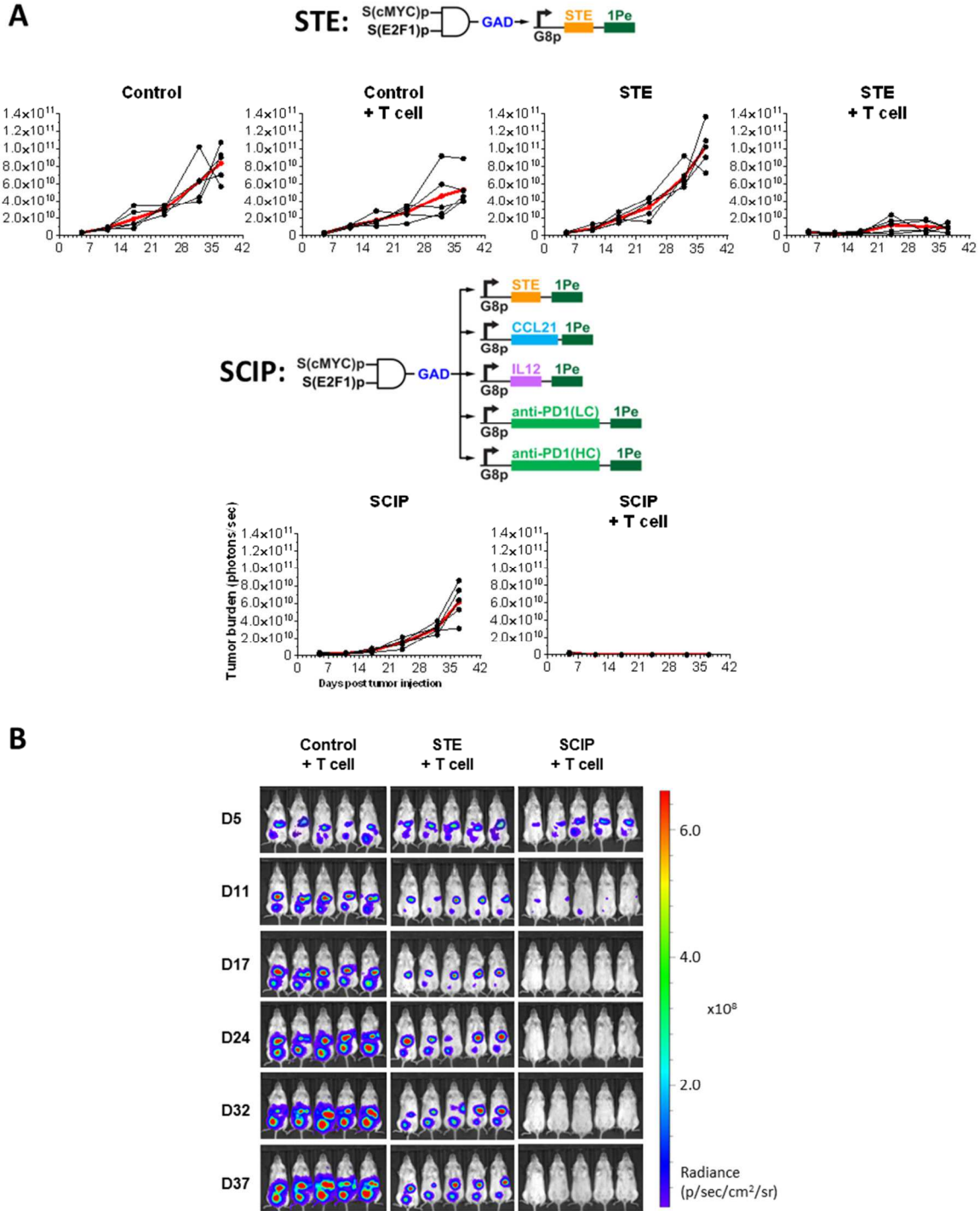


**Figure S5.** Combination immunotherapies triggered by the circuits significantly reduced tumor burden in an intraperitoneally disseminated ovarian cancer model within NSG mice periodically injected with human T cells, related to Figure 7.

**(A)** Tumor burden of individual mice (black) and mean (red) of each tested group (N = 5 biological replicates). X-axes denote days post tumor injection, Y-axes denote tumor burden (photons/sec).

**(B)** *In vivo* tumor bioluminescence images of each mouse from day 5 (D5) to 37 (D37). This data corresponds to the experiment shown in Figure 7A-B.

**Figure S6**

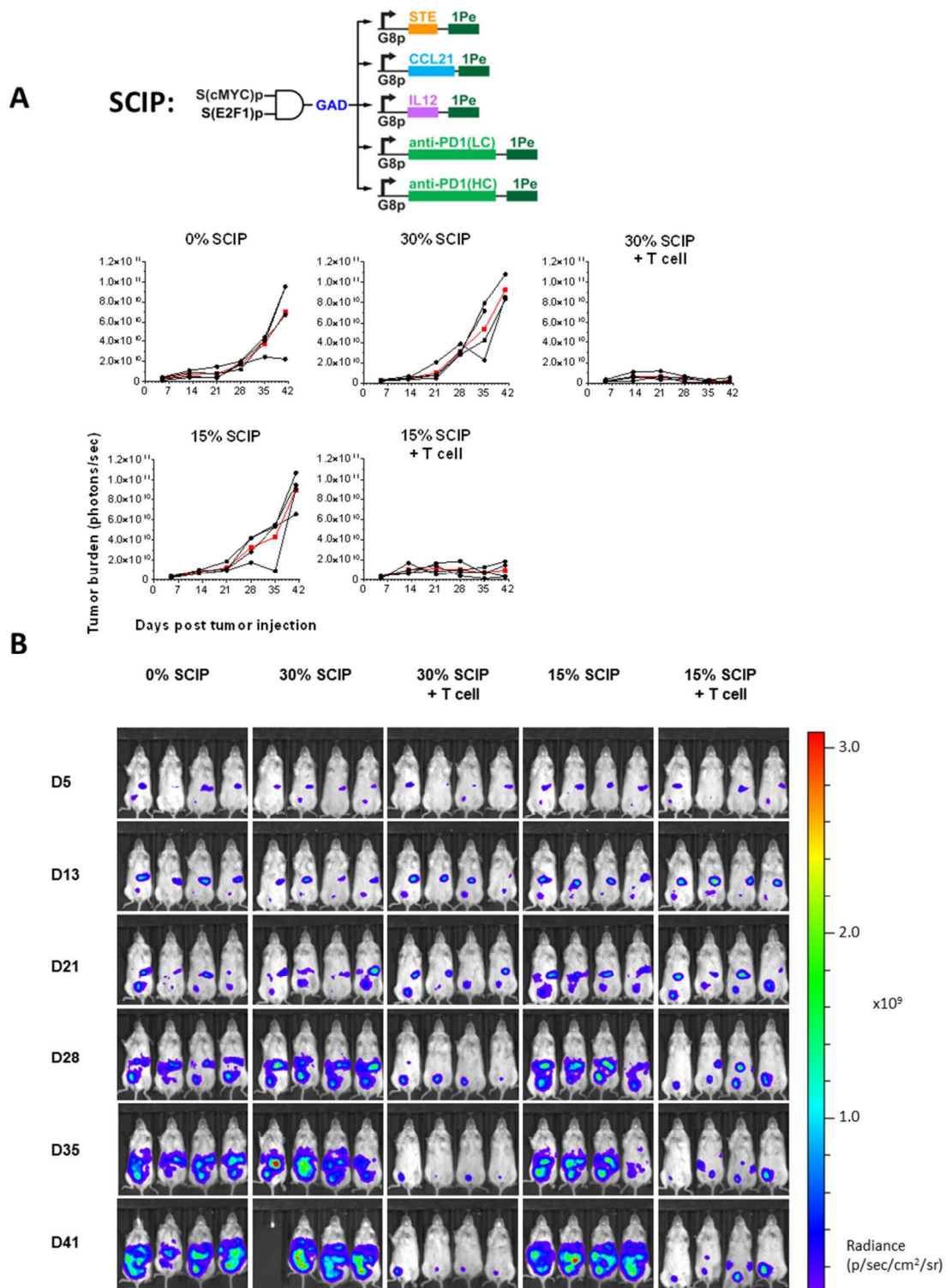


**Figure S6.** Robust therapeutic efficacy was achieved even only 15% of tumor cells were transduced with the SCIP-expressing circuit and then implanted into the peritoneal cavity of mice, related to Figure 7.

**(A)** Tumor burden of individual mice (black) and mean (red) of each tested group (N = 4 biological replicates). X-axes denote days post tumor injection, Y-axes denote tumor burden (photons/sec).

**(B)** *In vivo* tumor bioluminescence images of each mouse from day 5 (D5) to 41 (D41). This data corresponds to the experiment shown in Figure 7C-D.

**Figure S7.** Lentiviral delivery of SCIP circuit mediated robust therapeutic efficacy in an intraperitoneally disseminated human ovarian cancer model in mice, related to Figure 7.

**(B)** *In vivo* tumor bioluminescence images of each mouse from day 13 (D13) to 39 (D39). This data corresponds to the experiment shown in Figure 7E-F.

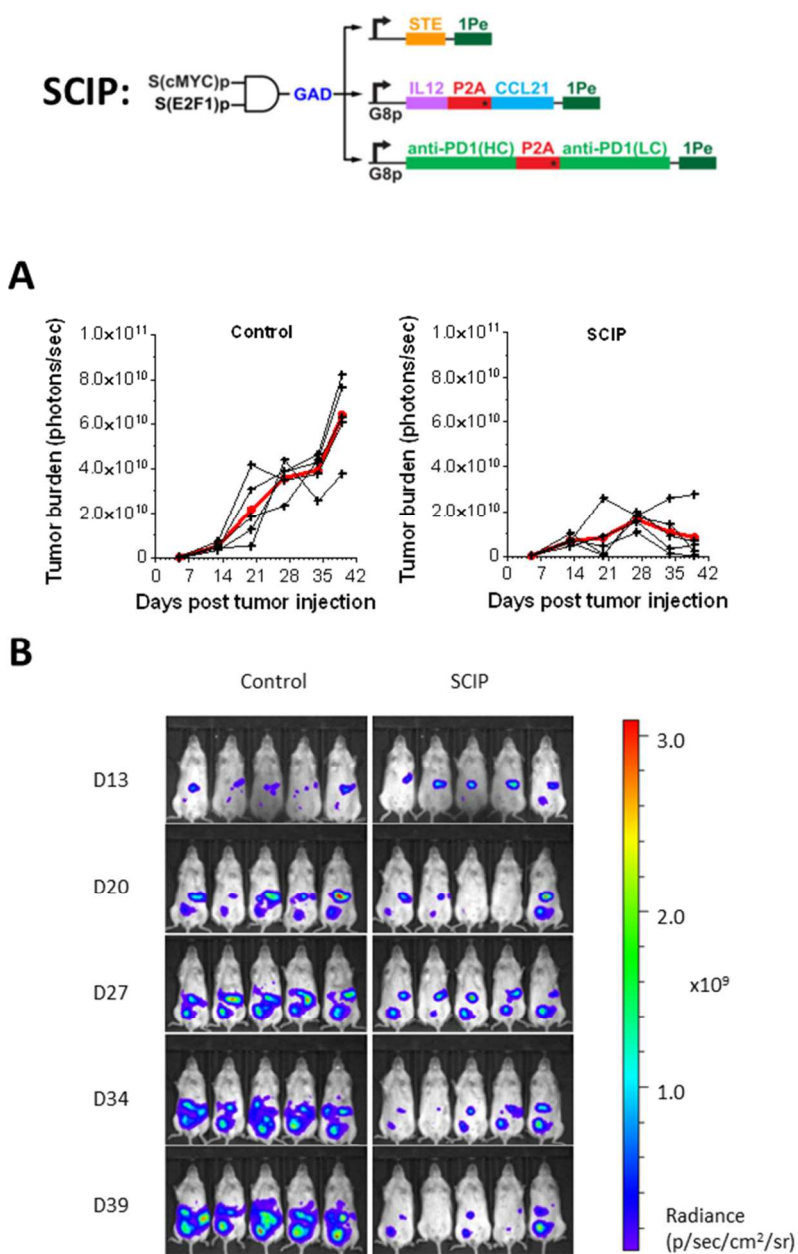
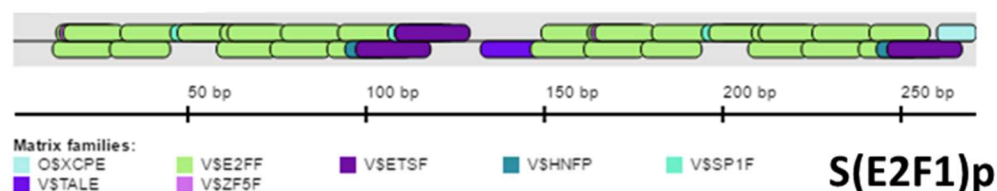
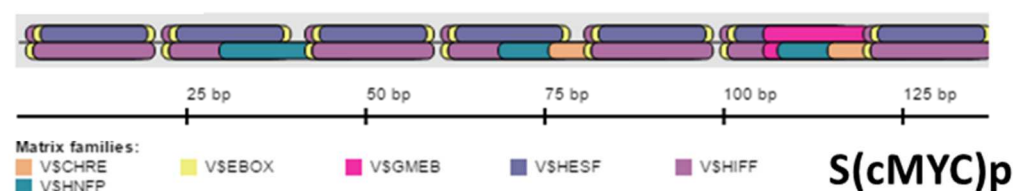
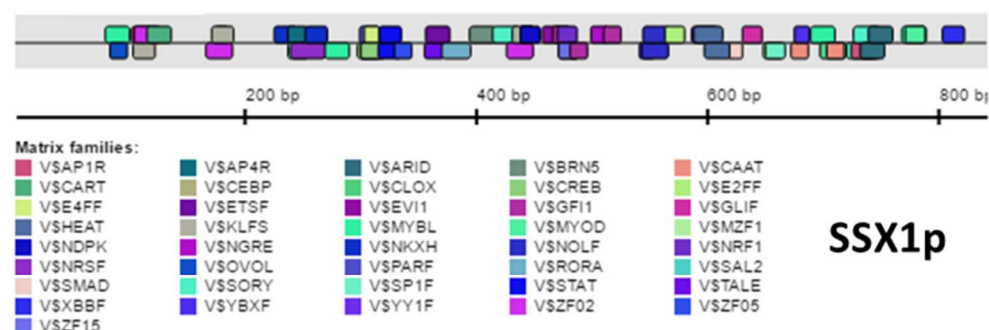


Table S1

	Total matches	TF families	Average matches per family	Max single-family matches	Max family % of total	Matches per 100bp
<b>SSX1</b>	66	41	1.6	4	6%	7.9
<b>H2A1</b>	82	40	2.1	9	11%	7.9
<b>S(cMYC)p</b>	49	6	8.2	14	29%	35.8
<b>S(E2F1)p</b>	44	7	6.3	29	66%	16.3



**Table S1.** Comparison of native and synthetic promoter sequences. We analyzed the sequences of representative native (H2A1p and SSX1p) and synthetic S(cMYC)p and S(E2F1)p cancer-specific promoters with MatInspector software to predict transcription factor binding sites (TF-BSs). **Total matches:** total number of TF-BSs identified; **TF families** (annotated as '*Matrix families*' by MatInspector): a group of different TFs that share very similar TF-BSs (i.e., Position Weighted Matrix) and biological function; **Average matches per family:** the mean number of TF-BSs per matrix family, calculated by the total number of identified TF-BSs divided by the number of different TF families; **Max single-family matches:** the maximum number of TF-BSs that belonged to a single TF family; **Max family % of total:** the percentage of 'Max single-family matches' out of the total number of TF-BSs identified; **Matches per 100bp:** the mean number of TF-BSs per 100bp in the promoter, used to normalize TF-BSs by promoter length. Bottom – graphical depiction of TF-BS families on promoter sequences. Tags indicate the location and orientation of each TF-BS (above and below the line for forward and reverse strands, respectively). Each different color denotes a different matrix family.



Table S2

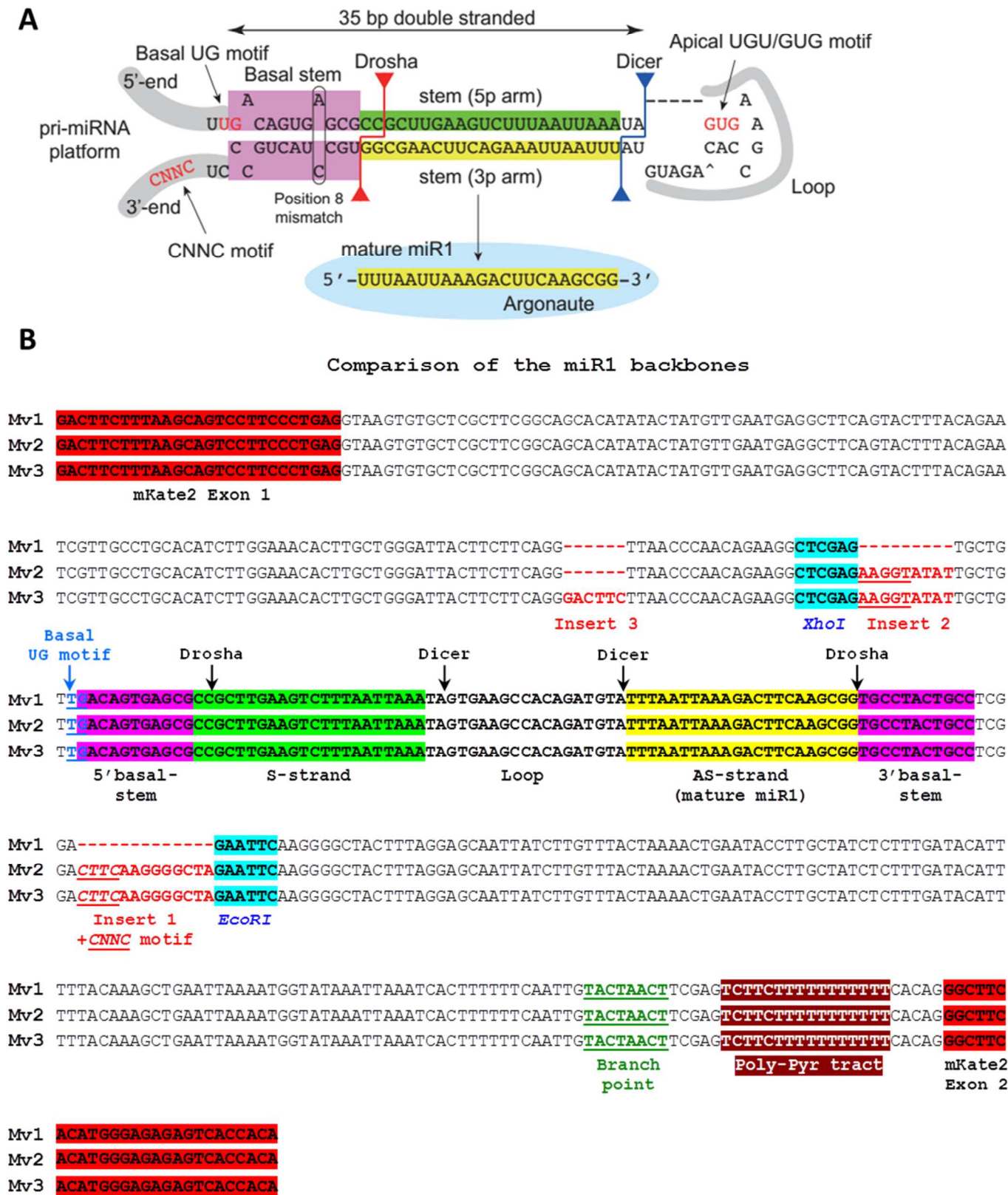


**Table S2.** Design and optimization of the miR1 expression cassette in *Module 1*, related to Figure 3.

**(A)** Structure of pri-miRNA in *Module 1*. Structural features of pri-miRNAs important for efficient pri-miRNA processing and frequently observed features in mammalian pri-miRNAs are indicated: basal UG motif, 35 bp double stranded stem structure, CNNC motif in the 3' flanking region, apical UGU/GUG motif in terminal loop and mismatch at position 8.

**(B)** Sequence alignment of pri-miRNA designs (Mv1, Mv2 and Mv3).



## Supplementary Information

### *Sponge optimization in Module 2*

We first optimized the miR1 binding-sites (miR1-BSs) in *Module 2* for maximal sponging efficiency. We designed 14 variants of miR1-BSs with different mismatches, insertions, and deletions compared to perfect-match miR1-BSs (Figure S1B-D). We measured the sponging efficiency of each variant by comparing mKate2 levels generated by *Module 1* in the presence of the *Module 2* sponge encoding 5 identical tandem miR1-BSs in the 3' UTR of ECFP versus no miR1-BSs (hereafter reported as “fold ON-OFF induction”). As an indication of miR1 binding to the sponge, we also expected to observe a decrease in ECFP expression in constructs where the 3' UTR of ECFP contained miR1-BSs versus no miR1-BSs. We used two highly active native promoters in HEK-293T cells, SSX1p (Gure et al., 1997) and H2A1p (Rogakou et al., 1998), to express *Module 1* and *Module 2*, respectively. In HEK-293T cells, H2A1p, which expresses the sponge in *Module 2*, is >3-fold stronger than SSX1p, which expresses *Module 1* (Figure S1A). Thus, the *Module 2* sponge transcript concentrations were expected to be in excess compared to the *Module 1* transcript, which ensured enhanced sponging efficiency. When we tested a sponge transcript with perfect match to miR1 generated by *Module 1*, we found a 80% decrease in the levels of ECFP, even though only a 33% decrease was expected due to the 1:3 ratio of miR1:sponge transcript concentrations. This phenomenon may reflect recycling of miRNA molecules following target transcript inhibition, which is especially efficient for perfect-match binding sites (Baccarini et al., 2011) (Figure S1D).

We calculated the binding efficiency of miR1 to its corresponding binding sites in the sponge ( $\Delta\Delta G$ ) with a previously described model (Kertesz et al., 2007), but we found that  $\Delta\Delta G$  did not predict sponging efficiency (Figure S1B). Specifically, calculations for microRNA binding efficiencies to target sites were performed at: [http://genie.weizmann.ac.il/pubs/mir07/mir07\\_prediction.html](http://genie.weizmann.ac.il/pubs/mir07/mir07_prediction.html). For example, binding sites with perfect complementary to miR1 (Pe) had the strongest binding efficiency ( $\Delta\Delta G = -26$ ), but limited mKate2 activation (Figure S1C, 1.7-fold ON-OFF induction), which could be a result of efficient sponge transcript degradation due to perfect miRNA complementarity (Ebert and Sharp, 2010). A  $\Delta\Delta G = -15$  was calculated for several binding sites that contained various mismatches to miR1 that resulted in bulged complementarity to miR1 (Bv2, Bv4, Bv6 and Bv15). Yet, the

measured ON-OFF induction for these binding sites ranged from 1.25-fold (Bv15) to 2.62-fold (Bv2), which covered almost the entire dynamic range of mKate2 activation. miR1 binding site version Bv2 contained mismatches to nucleotides 9-12 of miR1 and exhibited the best sponging efficiency (2.6-fold mKate2 ON-OFF induction), likely because mismatches at these positions protect the sponge from Ago2-mediated degradation while allowing efficient miR1 binding by preserving seed sequence complementarity (Ebert and Sharp, 2010). We therefore used Bv2 for the sponge in further optimization of the circuit. Hereafter, we use the abbreviation ‘#B’ to refer to the number of tandem Bv2 binding sites separated by 5 bp spacers (for example, ‘5B’ refers to 5 Bv2 binding sites). Finally, we also observed that ECFP levels could not predict mKate2 activation. These results highlight the complexity of miRNA-mediated regulation, in which the complementarity of the miRNA to its cognate binding sites determines not only the inhibitory pathway to which the target mRNA is designated (mRNA cleavage, destabilization or translation inhibition), but also the rate of unloading of miRNAs from Ago2, which is enhanced by high complementarity of the miRNA to its target (De et al., 2013). While bulged BSs generally have better efficiency in shunting miRNAs compared to perfect match BSs, we believe that deriving optimized rules on how to introduce effective bulges will require additional studies.

We then tested how the number, spacing, location and, architecture of miR1 Bv2 binding sites in the sponge transcript, together with sponge expression levels, affect sponging efficiency. We observed 2.9 and 3.6-fold mKate2 ON-OFF induction when 5B versus 10B binding sites were encoded in the 3’ UTR of the *Module 2* sponge transcript expressed by H2A1p, respectively (Figure S2A, ***Sponge 1: H2A1p-ECFP-5B*** versus ***Sponge 4: H2A1p-ECFP-10B***). Switching the promoter in the sponge encoding the 5B binding sites from H2A1p to CMVp, a 4.3-fold stronger promoter compared to H2A1p (Figure S1A), resulted in a 6-fold ON-OFF induction in mKate2 levels (Figure S2A, ***Sponge 3: CMVp-ECFP-5B***). Therefore, increasing the sponge transcript concentration efficiently increases miR1 shunting, suggesting that the promoter selected to express *Module 2* should be stronger than the one selected to express *Module 1*. Switching the location of the 10B from the 3’ UTR to the 5’ UTR of ECFP in *Module 2* (***Sponge 4: H2A1p-ECFP-10B*** versus ***Sponge 5: H2A1p-10B-ECFP***) reduced the sponging efficacy from 3.6-fold mKate2 ON-OFF induction to 2.4-fold (Figure S2A), which suggests that the miR1-BS(B) were more accessible when encoded in the 3’ UTR of the mRNA rather than in the 5’ UTR. Interestingly, increasing the spacing between miR1-BSs located in the 3’ UTR of the

sponge transcript from 5 bp to 100 bp (*Sponge 2: H2A1p-ECFP-5B/100bp*) only mildly reduced the sponging efficiency from 2.9 to 2.3-fold mKate2 ON-OFF induction. Additionally, encoding 24 miR1-BSs in the loop of an RNA hairpin with previously described tough-decoy (TuD) architecture (2 miR1-BSs per loop, 12 loops overall, *Sponge 9: H2A1p-ECFP-12TuD* (Ebert and Sharp, 2010; Haraguchi et al., 2009) provided only 3.8-fold mKate2 ON-OFF induction (Figure S2A).

Finally, to increase the molar ratio of sponges produced from a given promoter, we designed a *Module 2* variant where 10B were encoded as an intron within an ECFP coding sequence in addition to 5B encoded in the 3'UTR of the transcript (Figure S2A). In this architecture, the donor and acceptor consensus sequences that flank the 10 intronic miR1-BS(B) were derived from a previously described synthetic intron (*Sponge 6: H2A1p-EC1-10B<sub>Cons-EC2-5B</sub>*) (Greber et al., 2008). Based on ECFP expression, this sponge was correctly spliced, thus producing ECFP mRNA that contained 5B and an intron with 10B. This sponge demonstrated ~4-fold mKate2 ON-OFF induction, slightly better than *Sponge 4: H2A1p-ECFP-10B*.

We designed an additional architecture in which the intronic consensus sequences that flank the 10B were derived from the ZRANB1 gene (Memczak et al., 2013) (*Sponge 7: H2A1p-EC1-10B<sub>ZRANB1</sub>-EC2-5B*). This design was supposed to generate a stable circular 10B exon and EC1/EC2-5B introns, thus disrupting ECFP expression. This architecture demonstrated enhanced sponging efficacy with ~6-fold mKate2 activation (Figure S2A-B) and did not produce ECFP signal. To test whether that the lack of ECFP signal was caused by the expected improper splicing, resulting in an impaired ECFP transcript, or because the transcript was not spliced at all, we generated an additional sponge in which the ZRANB1 splicing sequences were deleted (*Sponge 8: H2A1p-EC1-10B-EC2-5B*). *Sponge 8* demonstrated almost identical sponging efficacy as *Sponge 7* (Figure S2A), which supports the hypothesis that *Sponge 7* did not splice. Since *Sponge 7* and *Sponge 8*, which did not splice, demonstrated higher sponging efficiency than *Sponge 6*, which did splice, we concluded that intronically encoded miRNA sponges did not significantly contribute to sponging activity. Thus, *Sponge 7: H2A1p-EC1-10B<sub>ZRANB1</sub>-EC2-5B* architecture was chosen as the final 'optimized sponge' design for our circuit.

## ***miRNA backbone optimization in Module 1***

We hypothesized that our circuit performance could be optimized by enhancing miR1 production from *Module 1*. We therefore modified the pri-miRNA stems for efficient pri-miRNA processing (Figure S3A & Table S2) (Auyeung et al., 2013; Fellmann et al., 2013; Suzuki et al., 2015). Previous studies have described multiple features of pri-miRNA stems that promote Drosha-mediated pri-miRNA processing, including a UG motif at the base of the pri-miRNA hairpin, a narrow range of tolerable pri-miRNA stem lengths, a mismatched motif in the basal stem region, and a CNNC motif 16-18bp downstream to the Drosha processing site that is required for efficient SRp20-dependent processing of the pri-miRNAs (Auyeung et al., 2013; Fellmann et al., 2013). Our miR1 design Mv1 was based on a previously described intronically encoded synthetic miRNA (Greber et al., 2008; Nissim et al., 2014; Xie et al., 2011) derived from a miR-30 backbone (Fellmann et al., 2013). The *EcoRI* restriction site at position 231-236 was generated by mutating the original sequence of endogenous miR-30 from GACTTTC to GAATTC (where position 1 is the first intronic nucleotide following the splicing of *Module 1*). This point mutation disrupted an essential CNNC motif in the miRNA backbone and resulted in reduced pri-miRNA processing efficiency. The *XhoI* restriction site at position 128-133 was generated by mutating the original sequence of the endogenous miR-30 from CTAAAAG to CTCGGAG, which could further impair the pri-miRNA secondary structure.

We generated our Mv2 design by adding a CNNC motif (**CTTCAAGGGGCTA**) downstream to base pair 231 of Mv1 (*Insert 1*) and an additional insert (AAGGTATAT) downstream to base pair 133 of Mv1 (*Insert 2*) to improve the secondary pri-miRNA structure that was altered by the formation of the *XhoI* restriction site (Fellmann et al., 2013) (Figure S3A & Table S2). To generate our Mv3 design, we added an additional insert (GACTTC) downstream to base pair 111 of Mv1 (*Insert 3*) to improve the secondary pri-miRNA structure that was altered by the formation of the *EcoRI* restriction site (Fellmann et al., 2013) (Figure S3A & Table S2). This resulted in a pri-miRNA backbone similar to the optimized miR-E backbone, which is superior to the miR-30 backbone (Fellmann et al., 2013).

We compared miR1 production from each backbone by characterizing their efficiency at inhibiting mKate2 levels in the *Module 1* transcript, in which they were encoded, and ECFP levels in a *Module 2* mRNA containing 5 perfect match miR1-BSs (5Pe) (Figure S3B-E). As

reference, we used a control construct with no miR1-BSs (Figure S3B). Pri-miRNA Mv3 mediated a 93% decrease in ECFP expression in the *Module 2* construct with the 5Pe sponge compared to the control construct, which was superior to Mv1 (80% inhibition) and Mv2 (71% inhibition), demonstrating that pri-miRNA design can tune the efficiency of miR1 production. This data suggests that that miR1 production was more potent in Mv3 compared to Mv2 and Mv1.

We also validated the effects of the miR1 backbone on the efficiency of mKate2 production by measuring mKate2 activation levels in the presence of the optimized sponge in *Module 2* (Figure S3D-E). The absolute mKate2 signal in the OFF and ON states (e.g. mKate2 levels measured with control versus optimal sponge) were both affected by the pri-miRNA design: Mv1 exhibited an OFF-ON shift from ~1400 to ~8400 Mean Fluorescence Intensity (MFI) (5.8-fold activation ratio), Mv2 from ~170 to ~500 MFI (3-fold activation) and Mv3 from ~380 to ~2600 MFI (6.8-fold activation). Based on the ECFP repression data from comparing the 5Pe sponge to the control construct, we expected Mv3 to be more efficient at inhibiting mKate2 than Mv1 and Mv2 in the presence of the 5Pe sponge. However, Mv2 exhibited potent inhibition of mKate2 levels in both the OFF and ON states. This suggests that our modifications to the pri-miRNA design may not only affect the efficiency of miR1 production, but also other regulatory mechanisms. We hypothesize that these pri-miRNA modifications could modify the efficiency of existing splicing sites or may have added alternative splicing sites in the miRNA intron that could impair mKate2 production by alternative splicing. This hypothesis is supported by the fact that the pri-miRNAs in designs Mv2 and Mv3 include a potential splicing donor sequence AAGGT introduced by Insert 2, and that a potential donor site CAGGT in Mv1 and Mv2 was modified to CAGGG by Insert 3 in Mv3 (Table S2).

As noted in the main text, we selected the Mv3 architecture for further experimentation since it had low mKate2 level in OFF state and exhibited the highest fold-activation by the sponge in ON state.

Finally, the miRNA duplex sequence can be modified to promote asymmetric guide strand selectivity that favors miR1 production. The miR1 pri-miRNA is processed into a miRNA duplex capable producing both miR1 encoded by the duplex 3p arm and an alternative miRNA encoded by the duplex 5p arm (Table S2). The ratio of 3p (miR1):5p production is determined by

the superposed patterns of the 5'-end nucleotide identity and the thermodynamic stability of two miRNA duplex termini (Suzuki et al., 2015). Quantitative thermodynamic and sequence analysis of the miR1 duplex has shown that the 3p arm has 5'-uridine and a thermodynamically unstable 5'-end, whereas 5p arm has 5'-guanine and a thermodynamically stable 5'-end (Suzuki et al., 2015). This indicates that the miR1 duplex is optimized to produce mostly the 3p arm (e.g. miR1); thus, it was therefore not modified. Nevertheless, we note that asymmetric guide strand selectivity is an important consideration in designing synthetic miRNAs.

### ***Bioinformatics framework for synthetic promoters design***

We identified genes that were differentially expressed in human ovarian cancer cells compared to healthy tissues from the publicly available The Cancer Genome Atlas (TCGA) database (Bell et al., 2011) using R (version 3.0.2). We followed standard procedures to calculate differentially expressed genes between cancer cases compared to controls using t-test. The p-values were corrected for multiple testing using the Bonferroni correction. We then selected genes that were previously identified as transcription factors (TFs) from the literature (Vaquerizas et al., 2009; Wingender et al., 2013). From these genes, we selected the ones that were hypomethylated in cancer. For that purpose, we used the publicly available database of DNA Methylation and gene expression in Human Cancer MethHC (Huang et al., 2015). This database provides the most hyper- and hypomethylated genes for different cancers. We selected TF genes with the most hypomethylated promoter regions using default settings. TF expression in OVCAR8 cells was confirmed using the CCLE database (Barretina et al., 2012). We then determined the binding motifs for ovarian cancer-enriched TFs using GREAT, MEME, JASPAR and MOTIFMAP (Bailey et al., 2009; Daily et al., 2011; McLean et al., 2010; Sandelin et al., 2004) and assembled them into our synthetic promoters (Figure 4A-B).

### ***Analysis of Natural and Synthetic Promoters***

We analyzed promoter sequences using MatInspector software to predict transcription factor binding sites (TF-BSs) (Cartharius et al., 2005). We ran our analysis on two natural promoters (SSX1p, H2A1p) and two synthetic promoters (S(E2F1)p, S(cMYC)p) using core similarity 0.9 and matrix similarity optimized + 0.05. We examined individual TF-BSs as well as

TF-BS families (defined as TFs with highly similar TF-BS – for example, the binding sites for MYC, USF and Max were grouped as the family E-BOX). We found that the synthetic promoters had more predicted TF-BSs per 100bp. For example, S(cMYC)p contained 35.8 TF-BS matches per 100 bp while H2A1p and SSX1p contained ~7.9 TF-BS matches per 100bp. The synthetic promoters had matches to less TF-BS families (~6-7 different TF-BS families) compared with the natural promoters (~40-41 different TF-BS families). The synthetic promoters had more TF-BS matches for each of the different TF-BS families compared with the natural promoters. Furthermore, we identified the TF-BS family with the highest number of matches for each promoter, and found that the top TF-BS family for the synthetic promoters had more TF-BS matches than the natural promoters. For example, E2F TF-BS family was found to be 66% of the total predicted TF-BSs in S(E2F1)p and the E-BOX TF-BS family (corresponding to MYC, USF, MAX) were found to be 29% of the total predicted TF-BSs in S(cMYC)p. In contrast, the ZF5F (ZFP 161) TF-BS family was found to be only 11% of the total predicted TF-BSs in H2A1p while the MYBL (MYB) TF-BS family was found to be only 6% of the total predicted TF-BSs in SSX1p.

### ***Multi-output AND Gate optimization for Combinatorial Immunomodulation***

We first characterized the output levels of four distinct circuit states in OVCAR8 cells (Figure 5B). To do so, we encoded each module on separate lentiviruses and infected OVCAR8 cells with the corresponding *Module 3* architecture and either: (A) a negative control *Module 1* that expresses the non-specific transcription factor rtTA3 (*Module 1con*) and a negative control *Module 2* in which S(E2F1)p expresses ECFP without miR1-BS(B) (*Module 2con*) to model the scenario when neither cancer-specific promoters are active [0,0]; (B) *Module 1con* and *Module 2* to model the scenario when only S(E2F1)p is active [0,1]; (C) *Module 1* and *Module 2con* to model the scenario when only S(cMYC)p is active [1,0]; (D) *Module 1* and *Module 2* to model the scenario when both promoters are active [1,1].

The circuits expressed minimal mKate2 fluorescence in states [0,0] and [0,1]. In state [1,0], there was a low background mKate2 level that increased from 5 to 8 GAL4-BSs in the synthetic GALp and was attenuated with the presence of miR1-BS(Pe) in *Module 3* (Figure 5B).

211 Only when both input constructs were present (state [1,1]) did we observe a significantly  
212 increased mKate2 output. Furthermore, the mKate2 output level could be enhanced by increasing  
213 the number of GAL4-BSs in the *Module 3* synthetic promoter from 5 to 8 GAL4-BSs. Although  
214 adding perfect match miR1 binding sites in the 3' UTR of the mKate2 transcript decreased the  
215 basal and maximal output levels, it also improved fold-activation (G5-Pe, G8-Pe, and G14-Pe  
216 versus G5, G8, and G14, respectively). The G8-Pe circuit exhibited negligible mKate2 levels in  
217 states [0,0] and [0,1], and high 8-fold mKate2 activation in state [1,1] over the minimal mKate2  
218 expression in state [1,0], and was thus chosen for further use.